



HAL
open science

Synchrotron high-resolution XRD and thermal expansion of synthetic Mg calcites

Nicole Floquet, Daniel Vielzeuf, Vasile Heresanu, Didier Laporte, Jonathan Perrin

► **To cite this version:**

Nicole Floquet, Daniel Vielzeuf, Vasile Heresanu, Didier Laporte, Jonathan Perrin. Synchrotron high-resolution XRD and thermal expansion of synthetic Mg calcites. *Physics and Chemistry of Minerals*, 2020, 47 (48), 10.1007/s00269-020-01115-5 . hal-02975828

HAL Id: hal-02975828

<https://uca.hal.science/hal-02975828>

Submitted on 23 Oct 2020

HAL is a multi-disciplinary open access archive for the deposit and dissemination of scientific research documents, whether they are published or not. The documents may come from teaching and research institutions in France or abroad, or from public or private research centers.

L'archive ouverte pluridisciplinaire **HAL**, est destinée au dépôt et à la diffusion de documents scientifiques de niveau recherche, publiés ou non, émanant des établissements d'enseignement et de recherche français ou étrangers, des laboratoires publics ou privés.

1 **Synchrotron High-Resolution XRD and thermal expansion of synthetic Mg Calcites**

2 Nicole Floquet,^{*,a} Daniel Vielzeuf,^a Vasile Heresanu,^a Didier Laporte^b and Jonathan Perrin.^c

3

4 ^a Aix-Marseille University, CNRS, CINaM UMR7325, 13288 Marseille, France

5 ^b Université Clermont Auvergne, CNRS, IRD, OPGC, Laboratoire Magmas et Volcans, 63000
6 Clermont-Ferrand, France

7 ^c Synchrotron SOLEIL, BP 38, Saint-Aubin, Gif-sur-Yvette, France

8

9 * Corresponding author N. Floquet.

10 Address : CNRS, UMR7325, Aix-Marseille University, CINaM, 13288, Marseille, France.

11 E-mail addresses : floquet@cinam.univ-mrs.fr (N. Floquet) vielzeuf@cinam.univ-mrs.fr (D.
12 Vielzeuf), heresanu@cinam.univ-mrs.fr (V. Heresanu), didier.laporte@uca.fr (D. Laporte),
13 perrin@synchrotron-soleil.fr (J. Perrin).
14

15

16

16 Abstract :

17 The structural parameters and the thermal behavior of a complete series of Ca-Mg carbonates
18 synthesized at high pressure and temperature (1–1.5 GPa, 1273–1373 K) in the range 0-50
19 mol% MgCO₃ has been investigated by in situ powder synchrotron high-resolution X-ray
20 diffraction at ambient and up to 1073 K under self-controlled CO₂ partial pressure. The crystal
21 structures are disordered Mg calcite in the range 1- 41 mol% MgCO₃, and Ca dolomite at 49
22 mol% MgCO₃. New calibration curves of the cell parameters for the Mg content and thermal
23 expansion from ambient to 1073 K are given. Short range structural effects of cation
24 substitution and ordering and their thermal behavior as a function of Mg content were
25 identified from three sets of data: the peak broadening, the cell parameter strains and the
26 Raman band enlargements. Both intra- and inter-crystalline levels of compositional
27 heterogeneity are identified and allow splitting the Mg calcites into two groups: low and high-
28 Mg calcites. The low Mg calcites (up to 22 mol% MgCO₃) are homogeneous in Mg content with
29 short range ordering. High Mg calcite (up to 41 mol% MgCO₃) display domains with different
30 local ordering configurations and similar or slightly different Mg contents, and to which is
31 added a compositional variation between crystals, as determined by EMP, of the order of ±
32 0.8 mol% MgCO₃. The cation ordering in Ca-rich dolomites similarly occurs in high-Mg
33 synthetic calcites. The role of (CO₃)²⁻ group ordering is shown to be an important factor in the
34 formation of Ca-Mg carbonates.

35

36 **Key-words:** calcite-dolomite solid solution; RT and high-temperature X-ray diffraction; crystal
37 structure; short range cation order; long range cation order; thermal expansion.

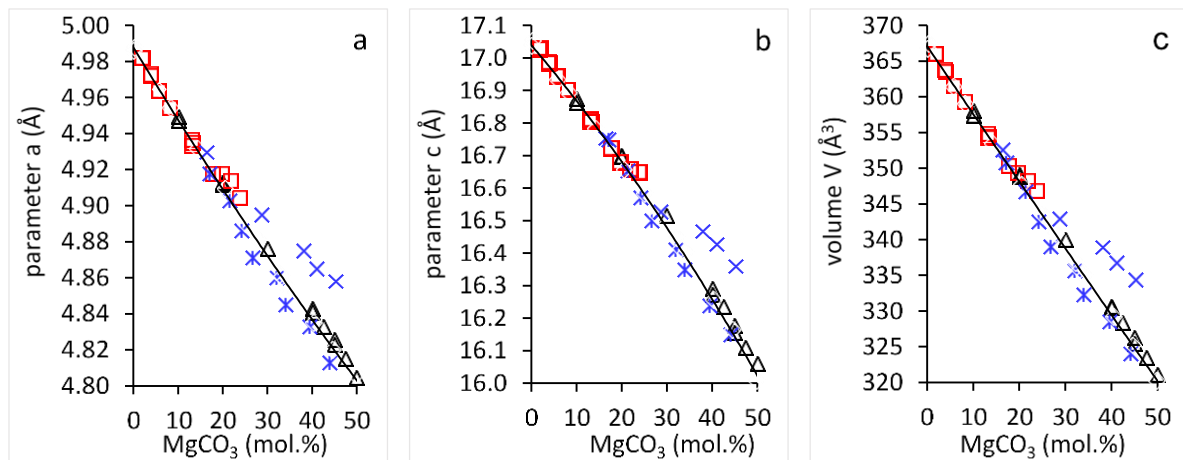
38

39 Introduction

40 Among all carbonate systems, Ca-Mg carbonates on the calcite dolomite join are the most
41 studied due to their importance as geological and industrial materials. Low to high Mg-calcites
42 are main components of many biominerals, whereas Ca-rich dolomites with Ca excess up to 6
43 mol% occur in sedimentary rocks of diverse environments and ages. Most natural carbonates
44 present morphology, structure, composition, stoichiometry, and/or cation ordering deviations
45 from the ideal crystalline structures of calcite and dolomite ([Deelman 2011](#); [Rodriguez-
46 Navarro et al. 2013](#)). Such features may contain information about crystal growth. They may
47 also reflect environmental factors that control Mg calcite and Ca dolomite formation and
48 transformation in biominerals and sedimentary rocks.

49 Optically clear natural (OCN) calcite, dolomite and synthetic crystals on the calcite-dolomite
50 join are commonly used as standards to study the physicochemical and structural properties
51 of natural carbonates. Synthesized Mg-calcites were produced either at high pressure and
52 temperature from solid mixtures ([Bischoff et al. 1983](#); [Goldsmith et al. 1958](#); [Goldsmith et al.
53 1961](#); [Jenkins et al. 2018](#)) or by crystallization in aqueous solutions under ambient pressure
54 and temperature ([Glover and Sippel 1967](#)) and references therein, ([Zhang et al. 2010](#)). As a
55 reference work, ([Bischoff et al. 1983](#)) synthesized up to 24 mol% MgCO₃ Mg-calcites at high
56 pressure (2, 10 and 15 kbar) and temperature (973K or 1273K), and characterized the products
57 by XRD and μ Raman spectroscopy. The Mg-calcites are reported as fully disordered calcite
58 structures and display a nonlinear, but smooth, variation of unit cell parameters and volume
59 with composition up to about 20 mol. % MgCO₃. ([Bischoff et al. 1983](#)) reported negative excess
60 volumes changing from negative to positive at 20 mol. % MgCO₃ ([Fig. 1](#)). ([Zhang et al. 2010](#))
61 indicate that the cell parameters of Mg calcites synthesized in aqueous solutions deviate from
62 a simple linear trend above 28 mol. % MgCO₃ ([Fig. 1](#)). ([Zhang et al. 2010](#)) considered that this
63 non-linear change of structural parameters is related to partially ordered arrangements of Mg
64 and Ca and twinning which are well known for compositions close to dolomite (([Reeder 1992](#);
65 [Rodriguez-Navarro et al. 2013](#); [Wenk et al. 1983](#)) and references therein). Thus, the
66 relationship between Ca-Mg structural ordering observed by transmission electron
67 microscopy ([Fang and Xu 2019](#); [Larsson and Christy 2008](#); [Meike et al. 1988](#); [Reksten 1990](#);
68 [Shen et al. 2014](#); [Van Tendeloo et al. 1985](#); [Wenk et al. 1991](#)) and the cell parameter variations
69 as a function of Mg content are still a matter of debate and require new structural studies of
70 high quality Mg calcites of known composition. Further evidence of structural ordering (or
71 not) can be obtained by studying the evolution of the crystal structure with temperature
72 through in situ heating experiments. An interesting relationship between structure and
73 physical property is observed in carbonates in terms of thermal expansion and its relationship
74 with anion group libration and cation octahedra composition ([Reeder and Markgraf 1986](#);
75 [Wang et al. 2018](#)). Indeed, calcite displays negative and positive thermal expansions of a and
76 c cell parameters, respectively, whereas dolomite and magnesite show positive, although
77 quite anisotropic, thermal expansions of both a and c parameters. Noting this fact, ([Markgraf](#)

78 [and Reeder 1985](#)) wondered about the thermal expansion of the a cell parameter in
79 magnesian calcites, and more specifically about the Ca:Mg ratio at which the thermal
80 expansion of the a cell parameter changes from negative to positive.



81
82 **Fig. 1** a , c and V parameters of synthetic calcites according to previous studies. Note the discrepancies
83 above 20 mol% MgCO₃. Black triangles: Goldsmith et al (1961); Blue stars: Erenburg (1963); blue
84 crosses: Zhang et al (2010); red squares: Bischoff et al (1983). The line in the V - X diagram corresponds
85 to the calibration curve of Jenkins (2018): $V (\text{Å}^3) = 366.788 - 0.9326 \times \text{mol\% MgCO}_3$
86
87

88 The present study is a follow-up from a previous one on the same synthetic carbonate
89 samples, already published by our group. The first study is a comprehensive characterization
90 by μ Raman spectroscopy giving accurate data (both in wavelength position and full width at
91 half maximum (FWHM) peaks of carbonate group vibration bands) on the local ordering of the
92 carbonate groups along the calcite-dolomite join ([Perrin et al. 2016](#)). The aims of the present
93 study are (1) to analyze the powder diffractograms obtained by synchrotron high-resolution
94 X-ray powder diffraction (HRXRPD), determine the cell parameters and identify the structural
95 short- and (or) long-range ordering (if any) of Ca-Mg carbonates in the range 0-50 mol%
96 MgCO₃; (2) characterize *in situ* the evolution with temperature of the crystal structure of
97 selected Mg calcites and determine their thermal expansion up to 1073 K under self-controlled
98 CO₂ partial pressure.

99

100 **Materials and Methods**

101 **Experimental syntheses**

102 The samples were synthesized at high pressure and high temperature in a piston cylinder
103 apparatus ([Perrin et al. 2016](#)). The Mg calcites cover the range 2 to 50 mol% MgCO₃ (2 and 5
104 mol% step intervals between 2-30 and 30-50 mol% MgCO₃, respectively). The starting
105 materials consist of pure synthetic calcite (Alfa Aesar) and natural magnesite from Brumado

106 (Bahia, Brazil). After desiccation in an oven at 383 K, about 60 mg of the mixture were loaded
107 in a 7 mm long by 5 mm outer-diameter gold capsule and welded shut. The gold capsule was
108 placed in a salt-glass assembly pressurized and heated for ~96 h in the piston-cylinder
109 apparatus, at 1273 K and 1 GPa for compositions in the range 2–30 mol% MgCO₃. For
110 compositions in the range 35–50 mol% MgCO₃, higher pressure and temperature were
111 selected (1373 K and 1.5 GPa) to avoid exsolution in the calcite-dolomite solvus as determined
112 by ([Goldsmith et al. 1961](#)). Large thick-walled capsules yielded sufficient quantity of crystalline
113 material in a single experiment to carry out different series of analyses while long run
114 durations (~4 days) favored attainment of textural and thermodynamic equilibrium. All runs
115 were quenched by the same procedure at high pressures, by cutting off the electrical power.
116 The quenching time was about 20 s from 1273 K to 573 K and 5 min to room temperature.
117 After the experiment, the run product was extracted from the capsule, part of it was mounted
118 in epoxy and polished for electron microprobe (EMP), scanning electron microscopy (SEM)
119 and μ Raman analyses ([Perrin et al. 2016](#)), while the remaining was ground and kept for X-ray
120 diffraction (XRD). OCN calcite, dolomite, and magnesite crystals were also analyzed to serve
121 as references. OCN calcite comes from a perfect rhombohedron of unknown origin. OCN
122 dolomite and OCN magnesite come from Azcárate quarry, Eugui, Esteribar (Spain), and
123 Brumado, Bahia (Brazil), respectively. Note that the number associated with the sample name
124 (e.g. MgCc2, MgCc50) refer to the nominal composition in mol% MgCO₃ in the starting
125 material. The actual concentrations measured by EMP are given in [Table 1](#).

126 **Analytical Methods**

127 ***Synchrotron High-Resolution X-ray Powder Diffraction***

128 HRXRPD of the samples was performed at the ID22 beamline of the European Synchrotron
129 Radiation Facility (ESRF, Grenoble, France). The instrument is equipped with a double-crystal
130 monochromator Si₍₁₁₁₎ and crystal analyzer optical elements in the incident and diffracted
131 beams, respectively. A description of the diffraction instrument is given by ([Fitch 2004](#)). The
132 setup allows high quality powder diffraction patterns with high signal/noise ratio, combined
133 with narrow peaks, accurate positions and intensities. The instrumental contribution to peak
134 width (FWHM) does not exceed 0.003° 2 θ . The typical resolution ($\Delta d/d$) is $\sim 10^{-4}$. Incident
135 beam size on the sample is typically 1.5 mm \times 1.5 mm. The selected wavelength $\lambda = 0.41068(1)$
136 Å (30 keV) was calibrated with Si standard NIST 640c (certified cell parameter $a = 5.4311946$
137 (92) Å). One mm outer-diameter quartz capillaries were filled with sample powder, then
138 sealed, mounted horizontally, and spun at 1000 rpm during data collection to improve particle
139 statistics. Data were collected in the 1° < 2 θ < 45° range, in continuous motion 5°/min, and
140 rebinned in 2 θ step of 0.003°. Data acquisition time was 30 min for each sample at room
141 temperature (RT) to ensure good counting statistics. For *in situ* heating measurements, the
142 capillaries were heated with a hot air blower mounted vertically, perpendicular to the
143 capillary. Temperature was controlled by a thermocouple located in the hot air stream. The

144 measurements (three recording patterns of 10 min at each T) were performed at RT, then in
 145 steps of 60 K from 353 to 1073 K (heating rate of 10 K/min) and again at room temperature
 146 after cooling.

Samples Name_nominal composition	Composition EMP MgCO ₃ (mol. %)	Proportion Weight %	Space Group	Unit cell parameters		Microstructural parameters		
				<i>a</i> (Å)	<i>c</i> (Å)	FWHM (1 0 4) 2θ (°)	size< <i>L</i> > (μ)	microstrain <ε> 10 ⁻³
P=1GPa T=1273 K								
MgCc_2	0.66 (0.05)		R3c	4.98708(9)	17.05868(4)	0.0076	0.911	0.053
MgCc_4	3.23 (0.10)			4.97620(1)	17.00054(5)	0.0066	1.008	0.144
MgCc_6	4.02 (0.12)			4.95942(2)	16.92903(9)	0.0074	0.874	0.188
MgCc_8	6.08 (0.12)			4.96344(1)	16.94464(5)	0.0141	0.822	0.138
MgCc_10	9.67 (0.30)			4.94726(2)	16.86430(9)	0.0089	0.930	0.370
MgCc_12	9.52 (0.13)			4.94731(1)	16.86683(5)	0.0085	1.083	0.186
MgCc_14-1	11.64 (0.68)			4.93507(1)	16.80922(8)	0.0107	1.346	0.226
MgCc_14-2	11.31 (0.22)			4.93805(1)	16.82313(8)	0.0108	0.957	0.291
MgCc_16	12.45 (0.21)			4.93596(1)	16.80992(5)	0.0071	0.952	0.224
MgCc_18	14.46 (0.14)			4.92730(1)	16.76702(7)	0.0073	1.023	0.117
MgCc_20	16.31 (0.27)			4.92161(2)	16.73950(8)	0.0080	0.886	0.163
MgCc_22	18.23 (0.26)			4.91308(1)	16.69584(8)	0.0092	0.925	0.140
MgCc_24	20.69 (0.27)			4.90156(1)	16.63502(5)	0.0078	1.305	0.188
MgCc_26	22.02 (0.40)			4.89639(1)	16.60686(8)	0.0103	1.011	0.158
MgCc_28	23.97 (0.26)	43		4.88237(4)	16.5271(2)	0.0108		
		36	4.88655(5)	16.5547(2)	0.0163			
		21	4.89116(4)	16.5811(2)	0.0187			
MgCc_30	25.69 (0.22)	28	4.87987(5)	16.5220(2)	0.0151*			
		42	4.87732(5)	16.5010(2)	0.0151*			
		30	4.87428(5)	16.4786(2)	0.0151*			
P=1.5GPa T=1373 K								
MgCc_35	28.25 (0.30)	31	4.87108(5)	16.4689(2)	0.0155*			
		29	4.86668(6)	16.4387(2)	0.0155*			
		21	4.86117(6)	16.4052(2)	0.0155*			
MgCc_40	37.77 (0.50)	18	4.83564(3)	16.26039(1)	0.0978			
		46	4.84199(3)	16.2942(1)0	0.0108*			
		25	4.83869(4)	16.2677(2)	0.0108*			
MgCc_45	41.43 (0.36)	29	4.83462(3)	16.2427(1)	0.0108*			
		31	4.82739(8)	16.2045(3)	0.0097*			
		21	4.82516(1)	16.1833(5)	0.0097*			
		48	4.82191(6)	16.1633(3)	0.0097*			
MgCc_50	49.23 (0.29)		R3	4.80585(1)	16.05064(5)	0.0085	1.580	0.196

147
 148 **Table 1** Refined unit cell parameters, microstructural parameters [FWHM broadening, size <*L*> and
 149 microstrain <ε>] of synthetic magnesian calcites and dolomite. (wavelength of λ = 0.41068(1) Å (30
 150 keV)) (standard deviation in brackets).* broadening coefficients of the pseudo-Voigt profile function
 151 constrained to the same values. Composition measured by EMP (Perrin et al., 2016)

152
 153 **HRXRPD Pattern Analysis**

154 **Cell parameters**

155 Both whole powder pattern and single peak analyses were performed with the Fullprof
 156 software suite (Rodriguez-Carvajal 1993). In the Rietveld refinements, the diffraction peak
 157 profiles were fitted with a pseudo-Voigt profile function and corrected for the asymmetry due
 158 to axial divergence (Rietveld 1969). All samples were refined in the rhombohedral system
 159 using the $R\bar{3}c$ space group for calcite, Mg-calcite and magnesite, and the $R\bar{3}$ space group for
 160 dolomite and Ca-dolomite. Starting atomic coordinates, cell parameters, and isotropic

161 temperature factors of calcite and magnesite are taken from ([Maslen et al. 1995](#)) while those
 162 of dolomite and Mg-calcite are from ([Althoff 1977](#)). The atomic composition of each powder
 163 sample was determined by EMP with a mean value and a standard deviation. Consequently,
 164 (1) the random occupancy of Ca and Mg into octahedral sites for Mg calcite samples were not
 165 refined but constrained to the EMP composition, (2) the CO₃ group was considered as a rigid
 166 structural unit. The C-O bond length was previously found to be very close to 1.284 Å for
 167 several carbonate phases, including magnesite and otavite ([Reeder 1983 ; Zemmann 1981](#)). The
 168 C-O bond length was fixed as a function of Mg content (n_{Mg}), between the C-O bond lengths
 169 in calcite ($n_{Mg} = 0$, $d(C-O)_{calcite} = 1.2864$ Å) and in dolomite ($n_{Mg} = 0.5$, $d(C-O)_{dolomite} = 1.2831$ Å).
 170 It was constrained according to the linear relation $d(C-O)_{MgCc} = -0.000068 \times n_{Mg} + 1.2864$ (with
 171 n_{Mg} : mol.% MgCO₃ determined by EMP reported on [Table 1](#)). The background function, scale
 172 factors, unit-cell parameters, Gaussian and Lorentzian broadening coefficients of the pseudo-
 173 Voigt profile function, and March-Dollase preferred orientation parameters were refined for
 174 each entire diffractogram. Atomic positions were refined only for OCN calcite, dolomite and
 175 magnesite. In the synthetic Mg calcites, where oxygen position and Ca and Mg occupations
 176 were constrained, typical agreement factors, χ^2 , R_p , and R_{wp} ranged from 3 to 13, 0.08 to 0.10,
 177 and 0.12 to 0.15, respectively.

178 *Long-range and short-range atom ordering*

179 The degree of order is of primary importance in the calcite-dolomite-magnesite system. As
 180 summarized by ([Putnis 1992](#)), the degree of order involves two different concepts.

181 *Long-range order* involves the occupancies of the sites averaged over the complete crystal. It
 182 is defined in terms of relative occupancy of non-equivalent sites. In the case of dolomite, the
 183 disordered state occurs on sites of two distinct layers, Ca layers labelled α and Mg layers
 184 labelled β . The degree of cation order is described by the order parameter s , defined as $s =$
 185 $(n_{Ca,\alpha} - n_{Ca,\beta}) / (n_{Ca,\alpha} + n_{Ca,\beta})$ where $n_{Ca,\alpha}$ and $n_{Ca,\beta}$ is the occupancy of Ca-type cations in Ca-type
 186 layers and Mg-type layers, respectively. The long-range order parameter equals 0 in the fully
 187 disordered state and 1 in the fully ordered state. Other equivalent formulations for the s order
 188 parameter were found for stoichiometric dolomites: $s = -1 + 2 \times n_{Ca,\alpha}$ ([Reeder and Wenk 1983](#))
 189 and for Ca-rich dolomite $s = (2 \times n_{Ca,\alpha} - n_{Ca,\beta}) / (2 - n_{Ca,\alpha} - n_{Ca,\beta})$ where $n_{Ca,\alpha}$ and $n_{Ca,\beta}$ are the
 190 occupancy of Ca-type cations in Ca-type layers and in Mg-type layers, respectively. ([Reeder](#)
 191 [2000](#)).

192 When the occupancy of Ca-type cations could not be refined, it is usual to calculate the long
 193 range order parameter in dolomite structure from the intensity of b -type peaks. In the
 194 dolomite diffractograms, the periodic layer arrangement of the non-equivalent sites gives rise
 195 to b -type ordering peaks [(1 0 1), (0 1 5), (0 2 1)] characteristic of the $R\bar{3}$ space group
 196 ([Goldsmith and Heard 1961](#); [Reeder and Nakajima 1982](#); [Deelman 1999](#)). In this case, the long-
 197 range order parameter is related to the intensities of normal (0 0 6) and b -type (0 1 5) peaks,
 198 and defined as $\sqrt{I_{015}/I_{006}}$ ([Zucchini et al. 2012](#)) and references therein). The order parameter
 199 $\sqrt{I_{015}/I_{006}}$ was determined from diffraction patterns computed with Fullprof for

200 stoichiometric dolomites (Supp. Mat. Fig. S1). From $n_{Ca,\alpha} = 1$ to 0, $\sqrt{(I_{015}/I_{006})} = 0.0058 \times (n_{Ca})^2$
201 $+ 1.0621 \times n_{Ca} + 0.0335$ where n_{Ca} is the Ca occupancy at its normal site in the dolomite
202 structure. The order parameter $\sqrt{(I_{015}/I_{006})}$ varies almost linearly between 1.1 and 0 from
203 fully ordered ($n_{Ca} = 1$) to fully disordered ($n_{Ca} = 0$) dolomite. In the present study, the linear
204 relation $\sqrt{(I_{015}/I_{006})} = 1.1 \times n_{Ca}$ was used to quantify the disordering in dolomite structures.
205 *Short-range order* was first introduced and theorized by Warren and Cowley (Warren et al.
206 1951; Cowley 1950, 1960). It involves the occupancies of the sites over a scale of a few Å. It is
207 defined by the probability that an atom is in the first coordination sphere surrounding an
208 arbitrary atom relatively to the random probability. In the case of Mg calcite, the disordered
209 state occurs on one set of equivalent cation (Ca,Mg) sites. The degree of short-range order (α)
210 is defined as $\alpha = 1 - P_{Mg}/n_{Mg} = 1 - P_{Ca}/n_{Ca}$ where $n_{Mg \text{ or } Ca}$ is the Mg (or Ca) occupancy fraction, i.e.
211 the random probability and $P_{Mg \text{ or } Ca}$ the probability of Mg (or Ca) atoms is within the first
212 coordination sphere surrounding a central Ca (or Mg) atom. In the random structure $\alpha = 0$,
213 while in the fully ordered structure $\alpha = 1$. In the Rietveld analysis of the Mg calcite powder
214 diffractograms, the substitution of Mg for Ca could not be refined, it was considered as fully
215 random and disordered. All kinds of short-range order being not considered, led to lower
216 agreement factors values. Besides, short-range order such as preferential occupancy of Ca and
217 Mg into octahedral sites within domains would generate variations of intensities and non-
218 uniform broadening of select families of reflections (Radha et al. 2007). In particular, ($h k l$)
219 stacking faults would selectively broaden the peaks due to the ($h k l$) family of reflections. The
220 heat treatment of Mg calcites is expected to induce lattice parameter distortions and Ca and
221 Mg re-ordering, but also change the average domain size and crystal lattice microstrain. For
222 these specific microstructural characterizations, each single peak in the diffractogram was
223 analyzed with the Winplotr program (Roisnel and Rodriguez-Carvajal 2001) and we used the
224 Williamson-Hall plot method (Williamson and Hall 1953) in which the broadened peak is
225 analyzed by a pseudo-Voigt function. The integrated intensity, coherent domain size $\langle L \rangle$ and
226 average microstrain values $\langle \epsilon \rangle$ are estimated from the refined profile width parameters. The
227 coherent domain size was determined using the (Scherrer 1918) formula: $\langle L \rangle = \lambda / \beta \cos(\theta)$
228 where λ , β , and θ are the wavelength, integral breath, and Bragg angle, respectively (Scherrer
229 1918). The microstrain effect is the variance of the lattice spacing ($\Delta d/d$) and the angular
230 dependence of the form is defined as $\Delta d/d = \beta / \tan(\theta)$ (Stokes and Wilson 1942).
231

232 **Results and interpretations**

233 **HRXRPD characterization of magnesian calcite syntheses**

234 ***Whole pattern analysis and cell parameters***

235 HRXRPD patterns of OCN calcite, OCN dolomite, and synthetic magnesian calcite MgCc24
236 (~20.7 mol% MgCO₃) are shown in Fig. 2. Note the narrowness of the peaks in the synthesized

237 materials. No phase other than Mg calcite and/or dolomite was detected. No indication of
 238 extended basal cation stacking order such as *b*-type ordering reflections characteristic of the
 239 ($R\bar{3}$) ordered structure of dolomite was found in the synthetic carbonates in the range 2-45
 240 mol% MgCO₃. MgCc50 with 49.2 mol% MgCO₃ is the only synthetic sample with this type of
 241 ordering reflections. (1 0 4) peaks of OCN calcite, OCN dolomite and synthetic samples in the
 242 range 2-50 mol% MgCO₃ are shown in Fig. 3. The plots of the (3 0 0) and (0 0 12) peaks
 243 (distinctive *a* and *c* basal reflections, respectively) are provided as supplementary materials
 244 (Supp. Mat. Fig. S2). The three figures show the same general features and allow identifying
 245 two groups of syntheses: a first group comprising the MgCc2 to MgCc26 samples is
 246 characterized by narrow and symmetric peaks, a second group from MgCc28 to MgCc45
 247 displays largely broadened and asymmetric peaks. The two groups will be referred to as low
 248 and high-Mg synthetic calcites, respectively. Diffractograms of the high-Mg synthetic calcite
 249 group can be analyzed in different ways: the peak broadening corresponds to a distribution
 250 curve of single phase Mg calcites with either 1) different Mg compositions, 2) different sizes
 251 and microdistortions (Ca/Mg disordering), or 3) different Mg compositions, sizes or
 252 microdistortions (Ca/Mg disordering). Table 1 reports the Rietveld refinement results of the
 253 simplest model involving three or four calcites with different compositions (and thus different
 254 cell parameters) and similar peak broadening. The origin of peak broadening will be discussed
 255 below. Refined unit cell parameters, microstructural parameters (FWHM broadening, size <L>
 256 and microstrain <ε>) for, synthetic Mg calcites, synthetic dolomite and OCN crystals are given
 257 in Tables 1 and 2. Unit-cell parameters and volumes obtained for all synthetic samples are
 258 shown as a function of their Mg contents in Fig. 4. For the high-Mg synthetic calcites, values
 259 of the three phases used in the refinement are plotted in the diagram. The *a* and *V* parameters
 260 show a small negative deviation from the Cc-Dol straight line, whereas the *c* parameter
 261 displays almost no deviation. These parameters can be fit with a second degree polynomial
 262 with R²>0.995:

$$263 \quad a \text{ (\AA)} = 4.9897 - 0.4747 \times (X_{\text{Mg}}) + 0.2037 \times (X_{\text{Mg}})^2$$

$$264 \quad c \text{ (\AA)} = 17.0643 - 2.1221 \times (X_{\text{Mg}}) + 0.0646 \times (X_{\text{Mg}})^2$$

$$265 \quad V \text{ (\AA}^3\text{)} = 367.9028 - 114.8121 \times (X_{\text{Mg}}) + 38.4623 \times (X_{\text{Mg}})^2$$

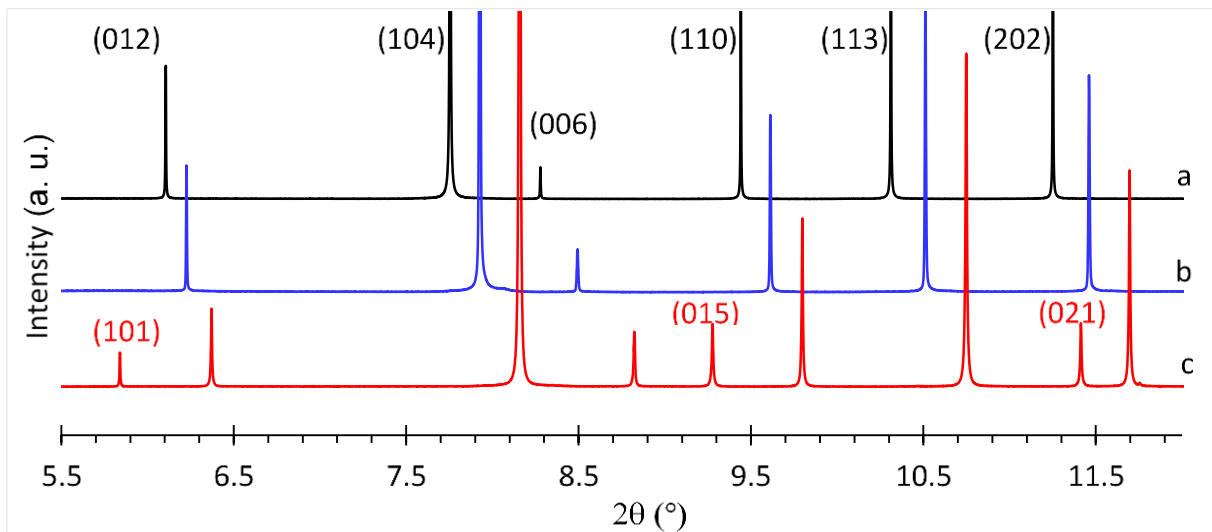
266 (X_{Mg} : mole fraction of MgCO₃ in the carbonate).

267 The fitting curves are shown in Fig.4. As stated by (Reeder 1983), $d_{(1\ 0\ 4)}$ has long been used to
 268 determine the Mg content of rhombohedral carbonates. In the present study the following
 269 relationship is determined:

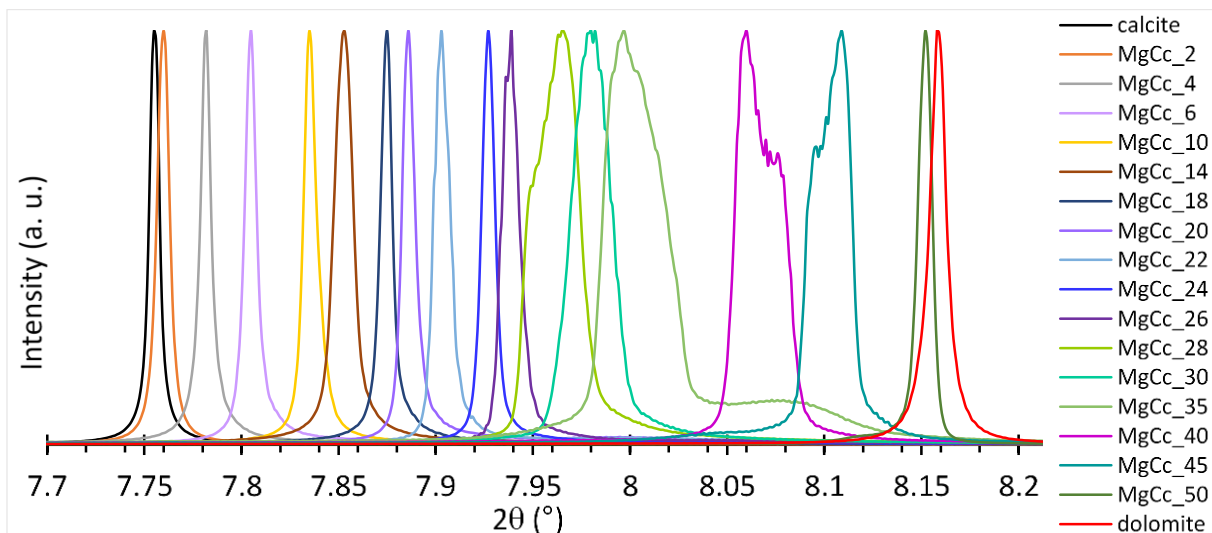
$$270 \quad d_{(1\ 0\ 4)} \text{ (\AA)} = -0.003032 \times (X_{\text{Mg}}) + 3.033503 \text{ (R}^2 = 0.994\text{)}$$

271
 272 It should be noted that $d_{(1\ 0\ 4)}$ does not provide a unique description of the cell while lattice
 273 parameters do, and thus cell parameters should be preferred to determine Mg contents in Ca-
 274 Mg carbonates (Reeder 1983). For natural carbonates (including biominerals) that may

275 contain significant amounts of other components such as Fe, Mn, Sr, S, organic matrix, etc.,
 276 direct measurements of compositions (by EMP for instance) should be preferred.
 277 Note again that the substitution of Mg for Ca in Mg-calcite has been considered as fully
 278 random and disordered in this analysis of the entire diffractograms. A more precise structural
 279 model that would take into account preferential occupancy of Ca and Mg into octahedral sites
 280 within domains, would possibly lead to better agreement-factor values. However in the
 281 present state of our knowledge, too many variables remain undetermined to allow this type
 282 of modelling with reasonable degree of confidence.



283
 284 **Fig. 2** HRXRPD patterns of (a) OCN calcite (black), (b) synthetic magnesian calcite MgCc24 (blue) and
 285 (c) OCN dolomite (red) [wavelength of $\lambda = 0.41068(1) \text{ \AA}$ (30 keV)]. Bragg peaks in the range 5.5 to 12°
 286 (2θ). $R\bar{3}c$ space group reflections in black, and $R\bar{3}$ space group b -type ordering reflections in red
 287

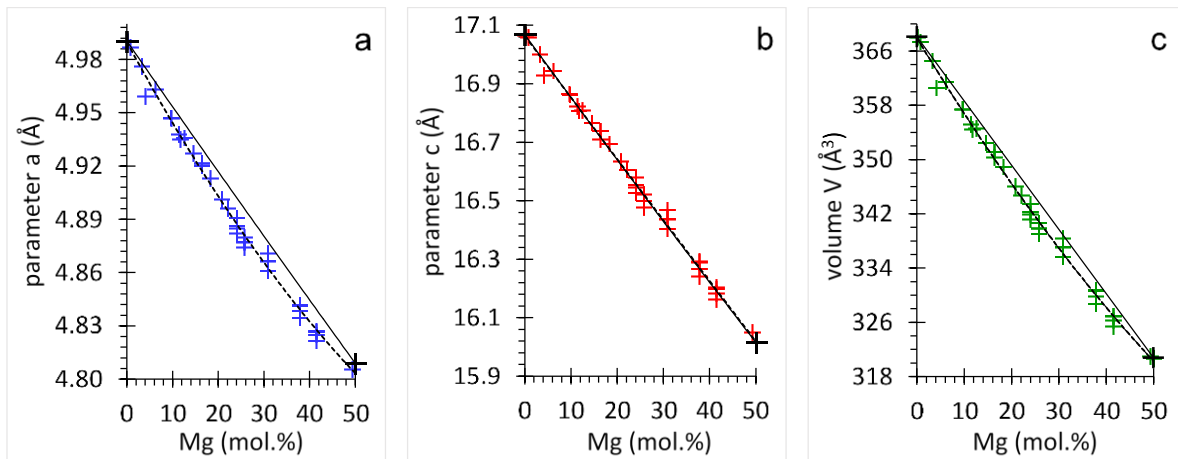


288
 289 **Fig. 3** Bragg (1 0 4) diffraction peaks of OCN calcite (black), synthetic magnesian calcites (MgCc2 to
 290 MgCc45), synthetic MgCc50 dolomite and OCN dolomite (red) [wavelength of $\lambda = 0.41068(1) \text{ \AA}$ (30 keV)]

291
292
293
294
295
296
297
298
299
300
301
302
303
304
305
306
307
308

Samples	Calcite	Dolomite	Magnesite
Unit cell parameters	Space Group R $\bar{3}c$	Space Group R $\bar{3}$	Space Group R $\bar{3}c$
a (Å)	4.98899(3)	4.80892(1)	4.63491(1)
c (Å)	17.05813(2)	16.01536(5)	15.02125(5)
FWHM(104) 2 θ (°)	0.0072	0.0091	0.0104
size <L> (μ)	0.541	1.156	0.717
microstrain < ϵ > 10 ⁻³	0.197	0.144	0.129
Conventional Rietveld R-factors			
Rp %	11.10	11.80	9.81
Rwp %	15.30	18.60	13.3
Rexp %	12.61	9.39	5.91
χ^2	1.47	3.92	5.06

Table 2 Refined unit cell parameters, microstructural parameters (FWHM broadening, size <L> and microstrain < ϵ >) and conventional Rietveld R-factors for OCN calcite, dolomite, and magnesite [wavelength of $\lambda = 0.41068(1)$ Å (30 keV)] (Standard deviation in brackets)



309 **Fig. 4** Unit cell parameters and volume as function of Mg composition for OCN calcite, OCN dolomite
310 (black plus) and for synthetic carbonate (blue, red and green plus). Dashed line is the quadratic least-
311 square adjustment as discussed in the text. Solid line is the straight line between OCN calcite and OCN
312 dolomite

313

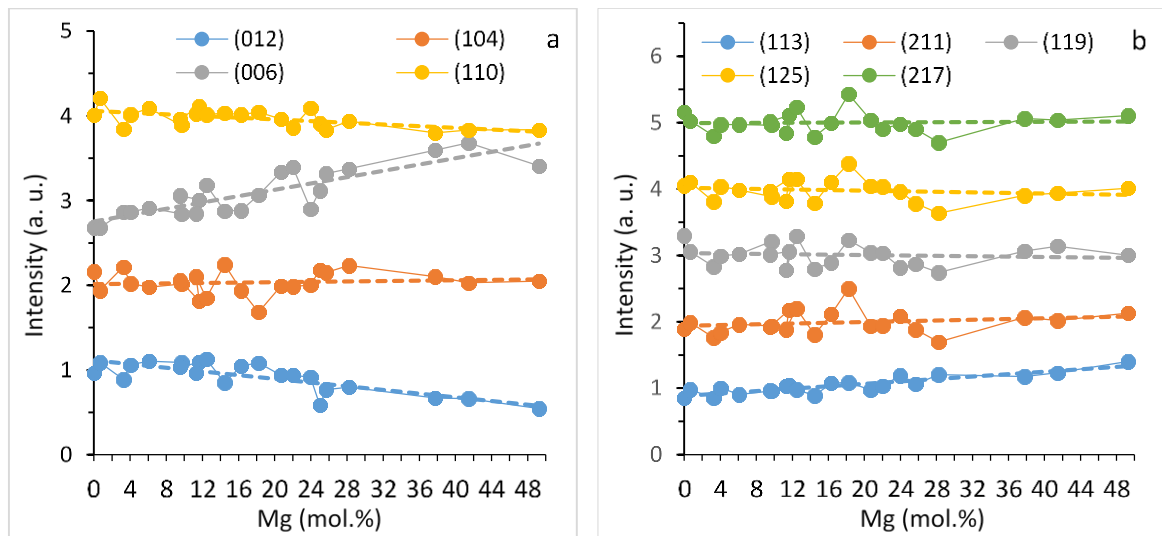
314 **Single peak analysis and microstructural parameters**

315

316 Short-range disorder in Mg calcites associated with the shift in position of atoms and
317 distortion of octahedral sites must generate variations of $(h k l) l = \text{even}$ intensities because of
318 large differences in X-ray scattering factors between calcium and magnesium atoms.
319 Misorientation of carbonate ions must generate variations of $(h k l) l = \text{odd}$ intensities. As far as
320 long-range order is concerned, the spatial extent and the structural nature of long range order
321 in Mg calcites domain must generate non-uniform widening of some families of reflections.
322 Below, both intensities and FWHM of the diffraction peaks are analyzed in order to
323 characterize both the structural short- and/or long-range order and the length of structural
324 coherence.

325 Intensities of several first ($h k l$) peaks for even and odd (l)s are shown in Figs. 5a and 5b as a
 326 function of Mg contents, and they are compared to those calculated from randomly
 327 disordered Mg calcite structure. Intensities of all ($h k l$) peaks vary linearly as a function of Mg
 328 content. No particular ($h k l$) intensity variation as a function of Mg content is observed. Some
 329 of them increase while others decrease. The deviations from linearity (SD = 0.10) are small
 330 and not correlated to Mg content and ($h k l$) families. A small deviation could be attributed to
 331 random distribution of structural distortions such as locally restricted cation ordering and
 332 anion positional disorder (off-planar tilting of the CO₃ groups) (Althoff 1977; Paquette and
 333 Reeder 1990). In the present case, the deviations are erratic and prevent refining a better
 334 structural model with confidence.

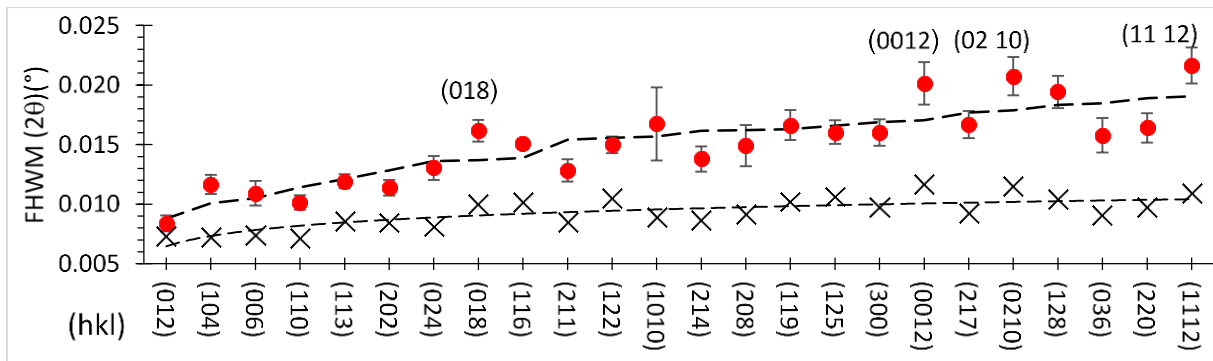
335



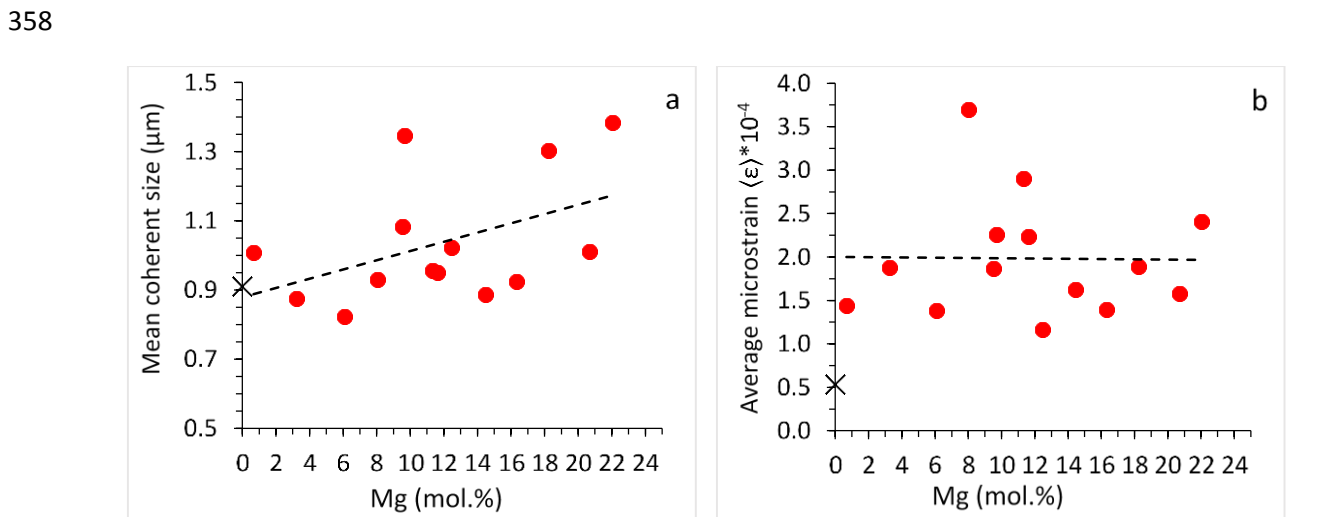
336 **Fig. 5** Observed intensities of ($h k l$) peaks a) l =even (distortion of octahedral sites); b) l =odd
 337 (misorientation of CO₃ groups) of synthetic carbonates as a function of Mg composition for synthetic
 338 carbonates (filled circles). The dashed line represents the intensities calculated for ideally disordered
 339 Mg calcites. All observed and calculated intensity are normalized to the same scale factor. Intensity axis
 340 is offset for each ($h k l$) for clarity
 341
 342

343 Concerning the FWHM, it has been mentioned earlier that two groups can be defined on the
 344 basis of peak FWHM differences, as observed in Fig. 3 (see also Supp. Mat. Fig. S2). In the low-
 345 Mg synthetic calcites (0-26 mol. % MgCO₃), the FWHM variation of each ($h k l$) peak as a
 346 function of Mg content is small (usually less than 0.3%) (SD in Fig. 6). The largest values and
 347 variations are for ($h k l$) peaks with large l values such as (1 0 10) (2 0 8) (0 0 12) (0 2 10) and
 348 (1 1 12). The ($h k l$) families with large l values are sensitive to local basal stacking disorder, but
 349 here again we must remain cautious as differences with variations observed in OCN calcite are
 350 small (Fig. 6). The structural distortions determined with the Williamson-Hall plot method are
 351 given in Table 1. The mean coherent domain size $\langle L \rangle$ [1.0 μm (SD = 0.2)] is similar to OCN calcite
 352 (Fig. 7a). However, the average microstrain $\langle \epsilon \rangle = 2 \times 10^{-4}$ (SD = 0.7×10^{-4}), that is 4 times higher

353 than in OCN calcite (Fig. 7b), could be related to the random distribution of structural
 354 distortions leading to small intensity deviations described above.



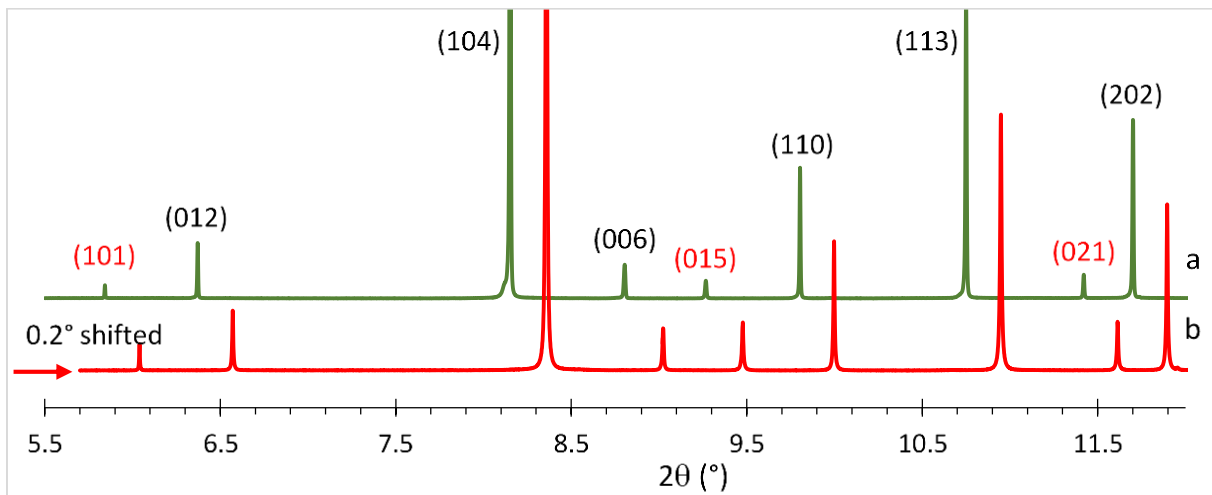
355
 356 **Fig. 6** FWHM of OCN calcite ($h k l$) peaks (black crosses). Mean FWHM of ($h k l$) peaks of 13 samples
 357 of synthetic low-Mg carbonates (MgCc2 to MgCc26) (red dots, vertical bars are standard deviations)



359 **Fig. 7** a) Mean coherent domain size $\langle L \rangle$; b) average microstrain values $\langle \epsilon \rangle$ calculated by the Williamson-
 360 Hall plot method for OCN calcite (black crosses) and for low-Mg synthetic carbonates (MgCc2 to
 361 MgCc26) (red dots). Dashed lines are linear least-square fitting curves

362 In the case of high-Mg synthetic calcites, the FWHM of the diffraction peaks are three to four
 363 time larger than low-Mg calcites (Fig. 3, Supp. Mat. Fig. S2). In addition, the peaks are
 364 asymmetric whatever the Mg content, and in a similar way for each ($h k l$) peak family. Thus,
 365 the FWHM broadening cannot be interpreted in terms of domain size and microstructural
 366 defects but rather in terms of coexistence of tiny domains with different compositions in a
 367 single crystal (Table 1). This interpretation will be developed in the discussion below.

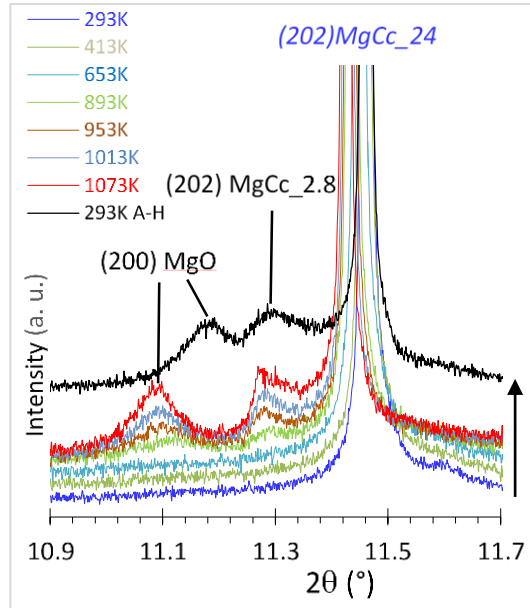
368 Special emphasis must be put on the MgCc50 sample that shows the characteristic
 369 superlattice peaks of dolomite. In this case and compared with OCN dolomite, no FWHM
 370 broadening of the $(h k l)$ peaks indicative of disordered stacking sequences is observed (Figs.
 371 3 and 8). FWHM of the $(1 0 4)$ peak (Fig. 3) and calculated size $\langle L \rangle$ and microstrain $\langle \epsilon \rangle$ are
 372 similar to those of OCN dolomite (Tables 1 and 2). For OCN dolomite, the long-range cation
 373 order parameter $\sqrt{(I_{015}/I_{006})}$ is equal to 1.07 whereas $\sqrt{(I_{015}/I_{006})}$ for MgCc50 dolomite equals
 374 0.64 (as a reminder, $\sqrt{(I_{015}/I_{006})}$ of a fully ordered dolomite equals 1.1). Thus, OCN dolomite
 375 is almost fully ordered with only 3% cation disorder, while the synthetic MgCc50 dolomite is
 376 characterized by 36% cation disorder. Such high disordered dolomite is expected at 1373 K
 377 since the critical temperature for the transition between long-range ordered and disordered
 378 dolomite has been located close to 1473 K (Goldsmith and Heard 1961). A similar degree of
 379 disorder ($s = 0.75$) is reported by (Reeder and Wenk 1983) in a natural dolomite, thermally
 380 treated at $T = 1373$ K and $P = 1.1$ GPa.



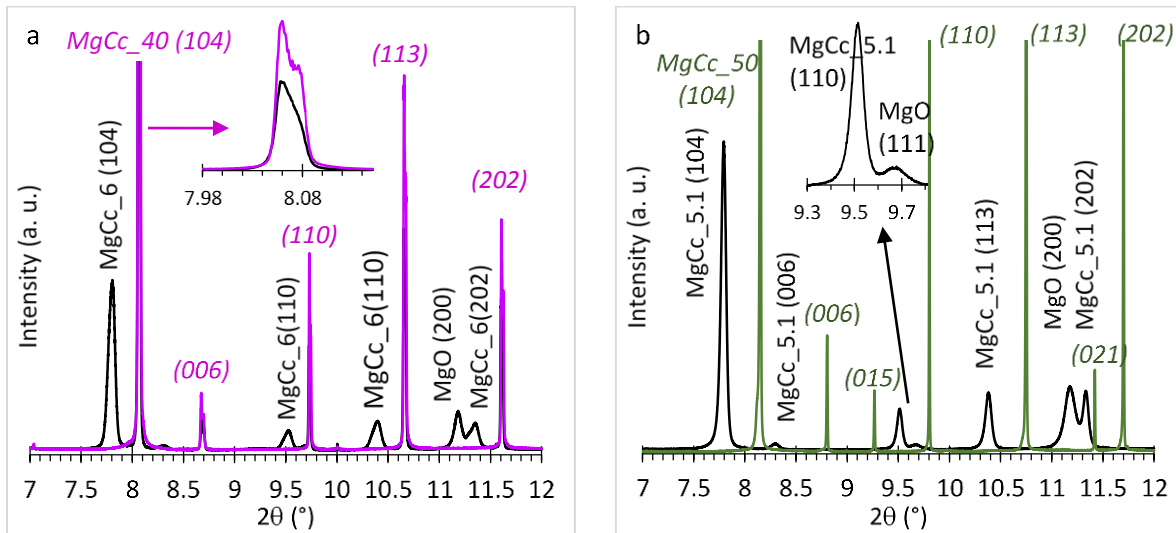
381 **Fig. 8** HRXRPD diffractograms of the OCN and synthetic MgCc50 dolomites (in red and green,
 382 respectively) (wavelength of $\lambda = 0.41068(1)$ Å (30 keV)). Bragg peaks in the 2θ range from 5.5 to 12 (°).
 383 Normal reflections and b -type ordering reflections for space group $R\bar{3}$ are noted in black and red,
 384 respectively. The red (OCN dolomite) has been shifted in 2θ for clarity

385 Thermally processed magnesian calcite syntheses

386 OCN dolomite, and the synthetic MgCc24, MgCc40, and MgCc50 samples have been thermally
 387 processed following the step-mode heating process previously used for OCN calcite and
 388 MgCc10 (Floquet et al. 2015). In this previous work, no phase decomposition of OCN calcite
 389 or MgCc10 was observed until 1073 K. As expected, the calcite unit cell showed contrasting
 390 thermal contraction and expansion for the a and c parameters, respectively. For Mg calcite
 391 MgCc10, the a cell parameter decreased until 673 K, then increased, while the c parameter
 392 expanded monotonically all along the temperature range. Figs. 9 and 10 display the XRD
 393 patterns collected at different temperatures for the MgCc24, MgCc40 and MgCc50 samples.



394 **Fig. 9** - Selected HRXRPD diffractograms in the 10.9 -11.7 2θ ($^{\circ}$) range of the synthetic MgCc24 sample
 395 recorded from RT to $T=1073$ K and then back to RT after heating (293 K A-H), showing (1) the (2 0 2)
 396 peaks of untransformed magnesian calcite (T in the range RT-653 K, indexes in italics) and partially
 397 decomposed product (at $T > 653$ K), and (2) the (2 0 0) peak of MgO resulting from partial decomposition
 398 (above 653 K). The black diffractogram collected at RT after annealing is shifted in intensity for clarity
 399 (black vertical arrow). [wavelength of $\lambda = 0.41068(1)$ Å (30 keV)]
 400



401 **Fig. 10** - a) HRXRPD patterns of synthetic MgCc40 recorded at RT (purple line, indexes in italics) and
 402 after annealing back to RT (black line). The original material (high-Mg calcite) is partially transformed
 403 into low-Mg calcite (~6.0 mol. % $MgCO_3$) and MgO; b) HRXRPD patterns of the synthetic dolomite
 404 MgCc50 recorded at RT before thermal processing (green line, and indexes in italics) and at RT after
 405 annealing at 1073 K (black line). The original dolomite has been totally transformed into low Mg calcite
 406 with ~ 5.1 mol.% $MgCO_3$ and MgO. [wavelength of $\lambda = 0.41068(1)$ Å (30 keV)]
 407
 408

409 **Thermal decomposition of Mg calcites and dolomite**

410
 411 Refined unit cell parameters and FWHM of (1 0 4) peaks of the samples as a function of
 412 temperature are given in **Table 3** and as supplementary data (**Supp. Mat. Tables S1 and S2**).
 413 Partial decomposition (PD) [or ‘half decomposition’ according to many authors (*e.g.* ([Valverde](#)
 414 [et al. 2015](#)) and refs therein)] meaning that an original magnesian calcite progressively
 415 decomposes at high temperature into a less magnesian calcite plus MgO, is observed for the
 416 three samples. The beginning temperature of partial decomposition (T_{PD}), decreases as the
 417 Mg content increases. For instance, MgCc24, MgCc40, MgCc50 start forming low Mg calcite
 418 (2.8 to 6 mol% MgCO₃) and periclase at T_{PD} of about 893 K, 833 K and 773 K, respectively (**Figs.**
 419 **9 and 10, Table 3**). After annealing at 1073 K for 20 min followed by cooling down to RT,
 420 MgCc24 and MgCc40 are only partially decomposed, whereas the dolomite sample (MgCc50)
 421 is completely transformed into low Mg calcite (~ 5.1 mol. % MgCO₃) and MgO. These
 422 observations are in great part in agreement with those of ([Reeder and Markgraf 1986](#)) who
 423 observed the beginning of dolomite decomposition at ~973 K and total transformation into
 424 Mg calcite at ~1023 K in partial CO₂ pressure. The average sizes of newly formed Mg calcite
 425 and periclase determined from the FWHM of the peaks using the Scherrer method, $\langle L \rangle \sim 80$
 426 and ~ 50 nm, respectively, are similar to those reported from XRD analysis of the thermal
 427 decomposition of dolomite. ([Hashimoto et al. 1980](#); [Rodriguez-Navarro et al. 2012](#))
 428

	Partial decomposition temperature (K)	Partial decomposition products at RT		Quantity Weight %	Unit cell parameters		FWHM (1 0 4)
		Formula	Mg mol.% ⁽¹⁾		a (Å)	c (Å)	2 θ (°)
MgCc24	893	MgCc24-ah	20.5	90.8	4.90154(1)	16.6345(5)	0.008
		MgCc	2.8	8.4	4.97000(1)	17.0500(5)	
		MgO		0.8	4.2523(9)		
MgCc40	833	MgCc40-1-ah	37.2	38.3	4.84346(4)	16.2870(2)	0.014
		MgCc40-2-ah	39.0	21.5	4.83823(4)	16.2435(2)	0.020
		MgCc	6.0	32.8	4.9500(1)	17.0172(5)	
		MgO		7.4	4.2144(7)		
MgCc50	773	MgCc	5.1	73.9	4.95435(1)	17.0359(5)	0.059 $\langle L \rangle = 80$ nm
		MgO		26.1	4.2164(2)		0.130 $\langle L \rangle = 55$ nm

429
 430 **Table 3** Partial decomposition temperature, composition, structural parameters (refined unit cell
 431 parameters) and microstructural parameters (FWHM broadening, size $\langle L \rangle$) of the decomposition
 432 products measured at RT after final step of annealing at 1073 K for MgCc24, MgCc40 and MgCc50.
 433 [wavelength of $\lambda = 0.41068(1)$ Å (30 keV)]. (ah: after heating)

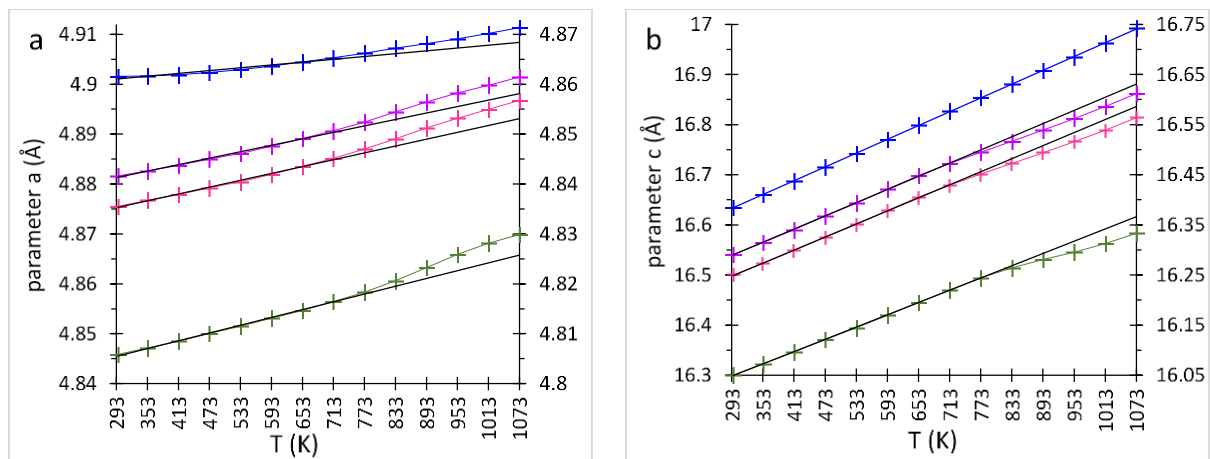
434 ⁽¹⁾ Mg contents calculated from the present study calibration curve that links the V parameter to the Mg
 435 content of synthetic Mg calcites (Fig. 4c)

436 437 **Variation of cell parameters with temperature**

438 The variations of the unit cell parameters of MgCc24, MgCc40 and MgCc50 in the range RT-
 439 1073 K are plotted in **Fig. 11**. Note that in the experiments undergoing partial decomposition,
 440 cell parameters were determined on the remaining magnesian calcite that did not undergo

441 partial decomposition. The unit cell shows a thermal expansion for both a and c parameters,
 442 even for MgCc24 with 20.7 mol% MgCO₃. The temperature dependence of a , c and V is not
 443 linear over the entire temperature range, as best observed in the c/a vs T plot (*Supp. Mat. Fig.*
 444 *S3*). Note that for MgCc40, a model with two Mg compositions (MgCc40-1 and MgCc40-2) has
 445 been used to refine the diffractogram, hence two curves are plotted in *Figs. 11, Supp. Mat.*
 446 *Fig. S3* for the MgCc40 experiment. The deviation from a linear expansion is positive for a , but
 447 negative for c , except for MgCc24 that shows a linear expansion for c . The c/a ratio of the unit
 448 cell deviates negatively from linearity at T_{dif} of about 653 K, 673 K and 773 K for MgCc24,
 449 MgCc40 and MgCc50, respectively (*Supp. Mat. Fig. S3*). A similar deviation occurs at ~ 673 K
 450 for MgCc10 due to the parabolic expansion of the a parameter ([Floquet et al. 2015](#)). The
 451 change of the thermal unit cell deformation starts at a temperature (T_{dif}) lower than the
 452 beginning of partial decomposition (T_{PD}) for Mg calcite, and at the same temperature for the
 453 synthetic dolomite ($T_{dif} \sim T_{PD}$).

454



455 **Fig. 11** Thermal expansion of the unit cell parameters a) a parameter; b) c parameter for synthetic
 456 MgCc24 (blue), MgCc40-1 and 2 (purple and pink) and MgCc50 (green), respectively

457 Above, two important temperatures are put forward: T_{dif} which is the temperature of the
 458 beginning of deviation from a linear expansion of the a , c (and V) parameter, and T_{PD} the
 459 temperature of beginning of partial half decomposition of Mg calcites. The physical meaning
 460 of T_{PD} is straightforward, as discussed above, while that of T_{dif} is not. On the basis of Raman
 461 characterizations, it has been argued that significant short-range Ca-Mg cation order is
 462 present in magnesian calcites that crystallized at 1273 K or 1373 K. Three reasons have been
 463 invoked: (1) the wavenumbers of magnesian calcites are close to the calcite–dolomite line
 464 (and not to calcite-magnesite), (2) the FWHM of the T, L, and ν_4 modes reach a maximum
 465 around 30 ± 5 mol% MgCO₃, and (3) the active mode (ν_2 , A_{2g}) in dolomite at 880 cm⁻¹ is
 466 observed in high-magnesian calcites above ~ 10 mol% MgCO₃ ([Perrin et al. 2016](#)). It should be
 467 noted also that short-range order greatly depends on temperature, it increases as
 468 temperature decreases. Thus, T_{dif} is interpreted as the temperature at which re-ordering (by
 469 diffusion) of calcium and magnesium atoms is activated to reach a more stable short-range

470 ordering configuration. For the studied Mg calcite samples, T_{dif} is lower than T_{PD} and the two
471 processes are expected to produce effects on Bragg peaks as a function of temperature, in
472 addition to the thermal vibrational effect reflected in the Debye-Waller factors. Actually, the
473 partial decomposition is mainly related to the decrease of all $(h k l)$ peak intensities. In
474 contrast, a short-range re-ordering should (1) produce thermal deviation excess of the cell
475 parameters and (2) lead to different variations of the $(h k l)$ peak intensities, and therefore
476 could be detected by the variation of the intensity ratio as function of temperature.

477 **Thermal expansion coefficients along the calcite-dolomite join**

478 High-temperature single crystal ([Markgraf and Reeder 1985](#); [Reeder and Markgraf 1986](#)) and
479 powder ([Antao et al. 2009](#); [De Aza et al. 2002](#); [Merlini et al. 2016](#)) diffraction experiments have
480 been conducted on calcite, dolomite and magnesite. The relative thermal expansion of the
481 cell parameters $a/a_{293\text{K}}$, $c/c_{293\text{K}}$ of OCN calcite, OCN magnesite and synthetic MgCc50 dolomite
482 are compared to those of these previous data in *Supp. Mat. Fig. S4*. The comparison shows (1)
483 a good agreement between OCN crystal data with powder diffraction experiments, but small
484 discrepancies with single crystal experiments, (2) a marked deviation at about 773 K (T_{dif}) for
485 synthetic MgCc50 dolomite compared to OCN dolomite. Similarly, the relative thermal
486 expansion of the cell parameters for OCN calcite, synthetic MgCc10, MgCc24 MgCc40, and
487 MgCc50 are presented in *Supp. Mat. Fig. S5*. The Fig. illustrates (1) the change of slope of the
488 a parameter as a function of temperature, from negative to positive, at about 10 mol% MgCO_3
489 (*Supp. Mat. Fig. S5a*), and (2) the deflection of slope of the c parameter as a function of
490 temperature, at about 653 K (T_{dif}) (*Supp. Mat. Fig. S5b*). The thermal coefficients obtained by
491 fitting the data to the usual second order polynomial curve are reported in [Table 4](#). The
492 coefficient of thermal expansion of parameter x ($x = a, c$ or V) $\alpha_x = (1/x)(dx/dT)$ is obtained
493 by differentiating the polynomial expression of the thermal expansion $x = f(T)$ and then
494 dividing by the x parameter ([Dubrovinsky 2002](#)).

495 The mean coefficient of thermal expansion over the temperature range from T_1 to T_2 is
496 expressed as $\overline{\alpha_x} = \int_{T_1}^{T_2} \alpha_x \times dT / \int_{T_1}^{T_2} dT$. Because of the noticeable deviation of the thermal
497 unit cell parameters at T_{dif} , the mean thermal expansion coefficients $\overline{\alpha_a}$, $\overline{\alpha_c}$ and $\overline{\alpha_V}$ are
498 calculated below and above T_{dif} , *i. e.* within two temperature ranges: 293 K-653 K (LT) and 653
499 K-1073 K (HT). The mean thermal expansion coefficients for the cell parameters are compared
500 to those of OCN calcite, magnesite and dolomite ([De Aza et al. 2002](#)) in [Fig. 12](#), no
501 measurements on OCN dolomite was realized by ourselves.

502 The particular features of the thermal expansion coefficients of calcite, dolomite and
503 magnesite, in both low- and high-T ranges, are 1) the negative $\overline{\alpha_a}$ of calcite and 2) all
504 coefficients of dolomite lie off of the calcite-magnesite line. These particularities were
505 comprehensively studied and discussed by ([Markgraf and Reeder 1985](#); [Reeder and Markgraf](#)
506 [1986](#)). In the Ca-Mg carbonate structure, the variation of the c parameter is related to the
507 variation of lateral oxygen bonds of the $(\text{Ca,Mg})\text{O}_6$ octahedra, while the variation of the a
508 parameter is related to the variation of basal oxygen bond which is limited by the resistance

	Unit cell parameters X (Å, Å ³)	$\alpha_{X653\text{ K}} (10^{-5} \text{ K}^{-1})$	$\alpha_{X923\text{ K}} (10^{-5} \text{ K}^{-1})$	X ₀	X ₁ (10 ⁻⁵ .K ⁻¹)	X ₂ (10 ⁻⁸ .K ⁻²)	References
		293 K<T<653 K	653 K<T<923 K				
Calcite	<i>a</i>	-0.462430	-0.35238646	4.991380	-2.992400	1.651090	Floquet 2015
	<i>c</i>	2.879871	3.09441674	17.053300	45.205000	10.152000	
	<i>V</i>	1.946290	2.37520437	367.94400	533.66000	456.60000	
MgCc10	<i>a</i>	-0.142341	-0.00435799	4.952266	-2.232100	1.670167	Floquet 2015
	<i>c</i>	2.765296	2.94037101	16.734160	41.563489	6.076303	
	<i>V</i>	2.477873	2.93080465	355.435213	554.827012	372.619230	
MgCc24	<i>a</i>	0.163899	0.25715705	4.900691	-0.096501	1.025117	
	<i>c</i>	2.766580	2.760282	16.498839	45.766889	0.114855	
	<i>V</i>	3.097712	3.28500822	343.171514	933.115278	153.983152	
MgCc40-1	<i>a</i>	0.434491	0.54096424	4.837140	1.158570	1.068103	
	<i>c</i>	2.701174	2.52356043	16.149320	49.132930	-5.866155	
	<i>V</i>	3.579215	3.62828059	327.244200	1148.113210	37.903090	
MgCc40-2	<i>a</i>	0.466206	0.57499191	4.831066	1.153930	1.189404	
	<i>c</i>	2.678535	2.48017763	16.237620	45.986310	-6.918950	
	<i>V</i>	3.620646	3.644942	325.567100	1156.664000	33.493130	
MgCc50	<i>a</i>	0.513846	0.643788	4.801714	0.968444	1.587677	
	<i>c</i>	2.519860	2.266482	15.899370	53.065870	-11.783200	
	<i>V</i>	3.557747	3.580010	317.479300	1182.483000	-11.375760	
Dolomite	<i>a</i>	0.546529	0.704501	4.803719	1.159773	1.652530	De Aza 2002
	<i>c</i>	2.410878	2.768941	15.924700	26.210036	13.255800	
	<i>V</i>	3.514414	4.209588	318.261370	667.070207	502.375754	
Magnesite	<i>a</i>	0.708000	0.770483	4.62600	2.828820	0.48015	
	<i>c</i>	2.371147	2.457921	14.91929	33.3164	2.568100	
	<i>V</i>	3.787114	3.975891	276.504425	952.21804	118.59584	

509

510 **Table 4** Thermal expansion coefficients of unit cell parameters obtained by fitting the data to the

511 expression $X(T) = X_0 + X_1 \times 10^{-5}T + X_2 \times 10^{-5}T^2$; $\bar{\alpha}_X = \left(\int_{T_1}^{T_2} \alpha_X \times dT / \int_{T_1}^{T_2} dT \right) 10^{-5}K^{-1}$ is the mean linear

512 thermal coefficient between T_1 and T_2 , where $\alpha_X = (1/x)(dx/dT)$ is the thermal expansion coefficient

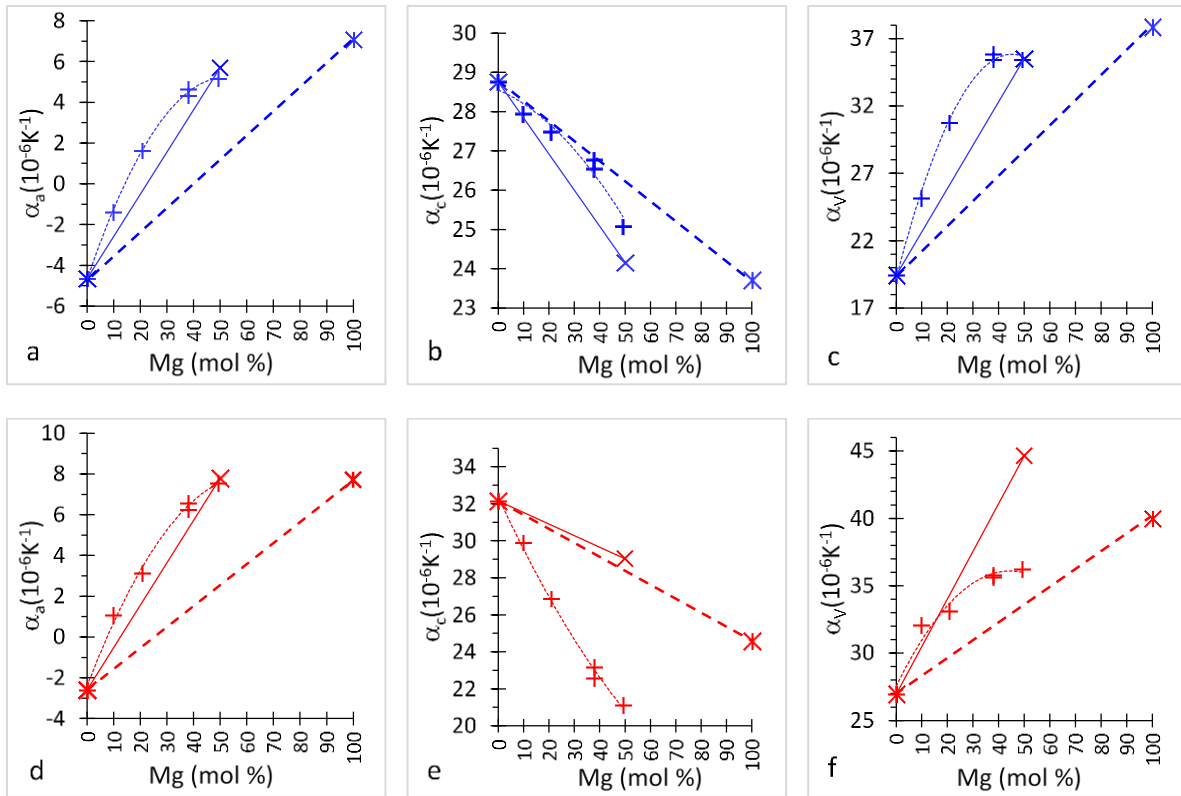
513 of parameter x ($x = a, c$ or V) and T is the temperature (K). No thermal measurements on OCN dolomite
514 was realized by ourselves

515
516 of rigid $(\text{CO}^{2-})_3$ groups. Accordingly, the thermal c expansion and a contraction in calcite is
517 related to the strong anisotropy of the thermal expansion of the CaO_6 octahedra and the large
518 magnitude of libration of the $(\text{CO}^{2-})_3$ group ([Markgraf and Reeder, 1985](#); [Reeder and Markgraf, 1986](#)).
519 In magnesite, characterized by the a and c thermal expansion, the thermal expansion
520 anisotropy of the MgO_6 octahedra is moderate and the dominant motion of $(\text{CO}^{2-})_3$ group is
521 the translation. In dolomite, the corner sharing between CaO_6 and MgO_6 octahedra in adjacent
522 layers induces a lack of anisotropy of the CaO_6 octahedra and a low amplitude of both libration
523 and translation motions of the $(\text{CO}^{2-})_3$ group. Thus, the shift of the cell thermal expansion of
524 dolomite from the calcite – magnesite line is explained by the perfect structural stacking
525 alternating Ca and Mg basal planes on both sides of each CO_3 plane. The systematic corner
526 sharing between CaO_6 and MgO_6 octahedra in dolomite is ruled out in the disordered
527 structures of MgCc calcites and dolomite. The thermal - structural relationships, as described
528 by ([Markgraf and Reeder 1985](#); [Reeder and Markgraf 1986](#)), imply that the thermal behavior
529 of the synthetic MgCc calcites and MgCc50 dolomite is dependent of the structural
530 arrangement of the CaO_6 and MgO_6 octahedra. The thermal coefficients are expected in the
531 calcite – dolomite line for fully disordered MgCc calcites. Thus, a thermal coefficient excess
532 from the calcite – dolomite line would be characteristic of the structural order of CaO_6 and
533 MgO_6 octahedra.

534 In the low- and high- T range ([Fig. 12](#)), the mean thermal expansion coefficients of the synthetic
535 MgCc calcites and MgCc50 dolomite lie off of both calcite-dolomite and calcite-magnesite
536 lines. In the low- T range ([Figs. 12 a to c](#)), a significant positive deviation from the calcite-
537 dolomite line is observed for the $\overline{\alpha}_a$ and $\overline{\alpha}_V$ coefficients, with a maximum deviation close to
538 25 mol% MgCO_3 for $\overline{\alpha}_a$. Conversely, the $\overline{\alpha}_c$ coefficients lie in between calcite - dolomite and
539 calcite – magnesite line. In the high- T range, positive deviation from calcite-dolomite line
540 occurs for the $\overline{\alpha}_a$ coefficients ([Fig. 12d](#)). On the contrary, large negative deviation are observed
541 for the $\overline{\alpha}_c$ and $\overline{\alpha}_V$ coefficients ([Figs. 12 e and f](#)).

542 For the synthetic MgCc calcites and MgCc50 dolomite, in the LT range 273 K-653 K, the thermal
543 expansion excess (with respect to the calcite-dolomite line) is positive for a , c and V
544 ($\Delta\overline{\alpha}_a=1\times 10^{-6}$, $\Delta\overline{\alpha}_c=1\times 10^{-6}$, $\Delta\overline{\alpha}_V=3\times 10^{-6}$). These results are consistent with the thermal-
545 structural relationships proposed by ([Markgraf and Reeder 1985](#); [Reeder and Markgraf 1986](#)),
546 and could be related to the state of order-disorder as do the cell parameters that are similarly
547 deviating from the calcite-dolomite line ([Fig. 4](#)). In the HT range, excess is unchanged for a
548 ($\Delta\overline{\alpha}_a=1\times 10^{-6}$) but largely negative for c and V ($\Delta\overline{\alpha}_c=-5\times 10^{-6}$, $\Delta\overline{\alpha}_V=-3\times 10^{-6}$). The differences
549 observed between the low- and high- T range comes from the positive and negative inflection
550 of the a and c parameters respectively, starting at T_{diff} in all synthetic MgCc ([Figs. 11 and Supp.](#)
551 [Mat. Fig. S3](#)) whereas not recorded in OCN dolomite powder ([De Aza et al. 2002](#); [Merlini et al.](#)
552 [2016](#)) and in dolomite single crystal ([Reeder and Markgraf 1986](#)) ([Supp. Mat. Fig. S4](#)).

553

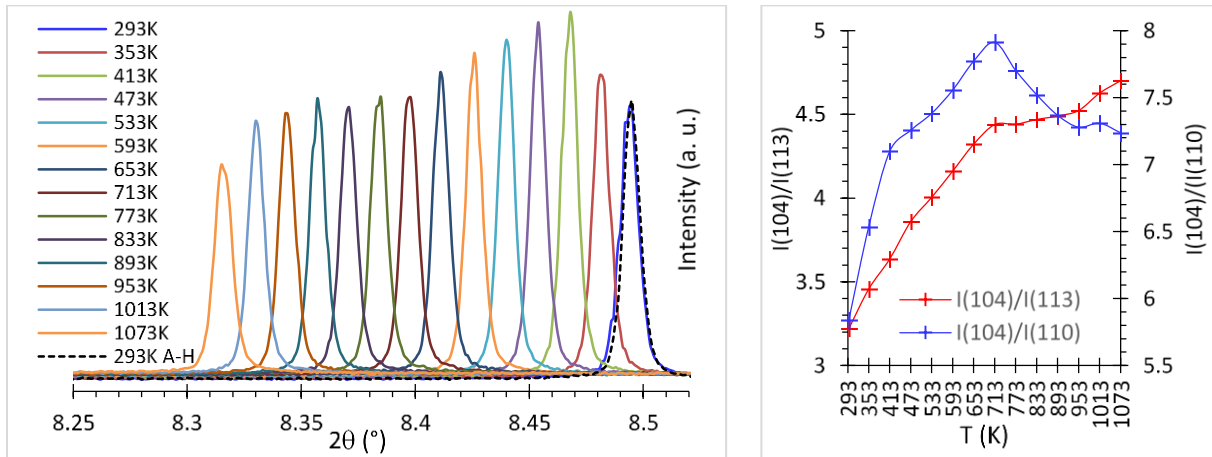


554
 555 **Fig. 12** Mean thermal expansion coefficients of the cell parameters α_a , α_c and α_v as a function of Mg
 556 content for OCN calcite and OCN magnesite (double crosses), natural dolomite (De Aza 2002)
 557 (crosses), and for synthetic MgCc10, MgCc24, MgCc40 and MgCc50 (plus) : a to c Low-temperature
 558 ranges (293-673 K) (blue) and d to f high-temperature ranges (653-923 K) (red)

559
 560 **Intensities and FWHMs of the Bragg peaks as a function of T . Interpretation of the data.**

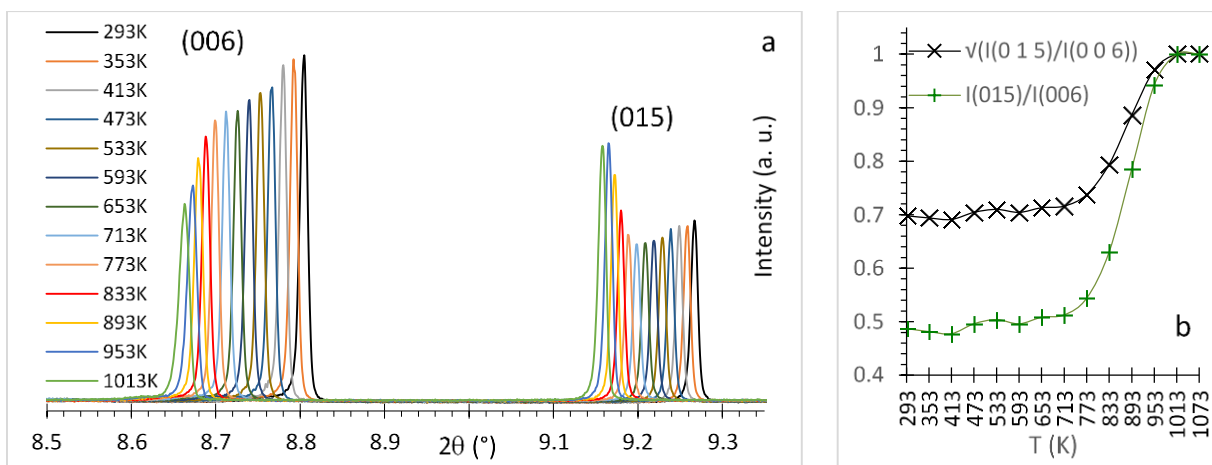
561 In the case of MgCc24 both intensity effects are detected. The variations of the (1 0 4) peak
 562 intensities as a function of T for MgCc24 are shown in Fig. 13a. The regular shift of the (1 0 4)
 563 peak towards lower 2θ values is due to the progressive change of cell parameters with
 564 temperature. Concerning intensities, different zones can be defined: (1) intensities increase
 565 between 293 K and 413 K, (2) intensities decrease regularly between 413 K and 713 K ($=T_{dif}$),
 566 (3) a plateau is observed between T_{dif} (713 K) and T_{PD} (953 K), (4) intensities decrease past T_{PD} .
 567 Interestingly, the two patterns determined at RT before (initial sample) and after annealing
 568 (remaining undecomposed sample) are almost identical (Supp. Mat. Table S1). Besides, the
 569 intensity ratio $I(1\ 0\ 4)/I(1\ 1\ 0)$ and $I(1\ 0\ 4)/I(1\ 1\ 3)$ shown in Fig. 13b displays two marked slope
 570 disruptions at 713 K and 953 K relevant to both diffusion and decomposition processes.
 571 However, no notable FWHM effect on the Bragg peaks was detected. The variations of ($h\ k\ l$)
 572 FWHMs as a function of T are unrelated to the Mg content of the samples, the variations
 573 among different samples are not significant (Supp. Mat. Table S1), and no irregularity is
 574 observed even for ($h\ k\ l$) peaks with large l values such as (0 1 8) (0 0 12) (0 2 10) and (1 1 12).

575 Concerning the synthetic dolomite MgCc50, T_{dif} equals T_{PD} and normal and b -type peak
 576 intensities display different behaviors. Normal peak intensities (e.g. 0 0 6) plotted in Fig. 14
 577 decrease progressively up to $T_{\text{dif}} = T_{\text{PD}} = 773$ K, then faster above T_{dif} . This observation is valid
 578 for all normal peaks. On the other hand, b -type peak intensities [e.g. (0 1 5)] decrease up to
 579 T_{dif} , then increase up to 1013 K (Fig. 14).



580

581 **Fig. 13** a) Bragg (1 0 4) diffraction peaks for MgCc24; b) Intensity ratio $I(1\ 0\ 4)/I(1\ 1\ 3)$ and $I(1\ 0\ 4)/I(1\ 1\ 0)$
 582 for MgCc24 (wavelength of $\lambda = 0.41068(1)$ Å (30 keV)) recorded from RT to $T=1073$ K. Note the
 583 slope breaks at 713 K and 953 K



584

585 **Fig. 14** a) HRXRPD patterns in the 2θ range corresponding to the (0 0 6) and (0 1 5) peaks; b) Intensity
 586 ratio $I(0\ 1\ 5)/I(0\ 0\ 6)$ (green plus) and $\sqrt{I(0\ 1\ 5)/I(0\ 0\ 6)}$ order parameter (black crosses) for MgCc50 (Ca-
 587 dolomite) from RT to $T=1073$ K (wavelength of $\lambda = 0.41068(1)$ Å (30 keV))

588 These data indicate that cation long-range reordering within the dolomite structure starts at
 589 773 K. The order parameter $\sqrt{I(0\ 1\ 5)/I(0\ 0\ 6)}$ shows that the MgCc50 dolomite is almost fully
 590 ordered at $T=1073$ K, with less than 10% cation disordering (Fig. 14b) which is not surprising
 591 since ordered dolomite is expected at 1073 K. (Hammouda et al. 2011; Zucchini et al. 2012).
 592 In addition, (Goldsmith et al. 1961; Reeder and Wenk 1983) concluded that cation ordering in

593 dolomite results in a decrease of c and a slight increase of a , thus a marked decrease of the
594 c/a ratio. Data reported above with c/a of MgCc50 deviating from linearity at T_{dif} (*Supp. Mat.*
595 *Fig. S3*) is interpreted as an effect of cation ordering activated by temperature, in a disordered
596 dolomite initially synthesized at 1373 K. Similarly to MgCc50, the changes of cell parameters
597 arising at $T_{\text{dif}} = 653$ K, 673 K for MgCc10, MgCc24 and MgCc40 are interpreted in terms of
598 ordering process in partially disordered Mg calcite samples synthesized at 1273 K or 1373 K.
599 Note that in the case of MgCc50, both short- and long-range ordering is implicated while in
600 more calcitic syntheses only short-range ordering would be implied. Summarizing, in the range
601 $RT-T_{\text{dif}}$, the variation of cell parameters is simply due to a thermal effect. Above T_{dif} , both
602 thermal effect and cation ordering affect the cell parameters. More interactive and interlinked
603 effects are expected once the partial decomposition starts.

604 Discussion

605

606 Comparison with previous data and interpretation of high-Mg calcite XRD patterns

607

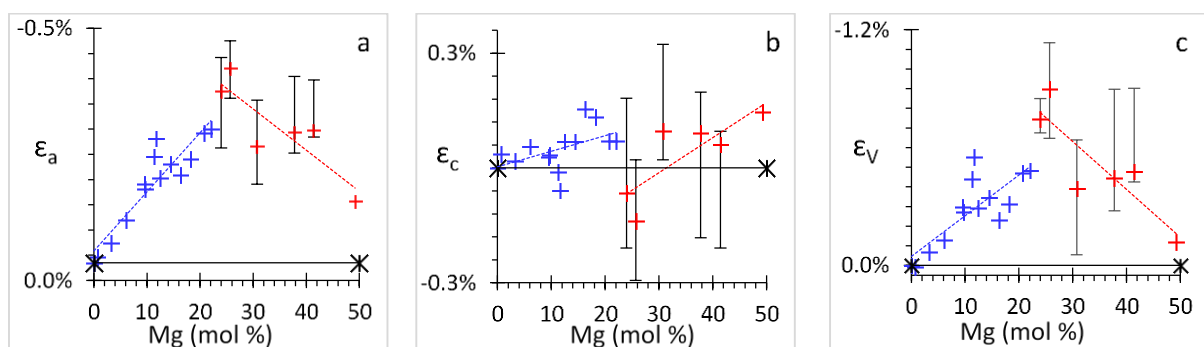
608 Our data are consistent with previous experimental studies ([Byrnes and Wyllie 1981](#);
609 [Goldsmith et al. 1955](#); [Goldsmith and Heard 1961](#); [Harker and Tuttle 1955](#); [Irving and Wyllie](#)
610 [1975](#); [Newton et al. 1969](#)) that predict a continuous (or almost continuous) solid solution
611 between CaCO_3 and $(\text{Ca}_{0.5}\text{Mg}_{0.5})\text{CO}_3$, in the pressure and temperature conditions of our
612 experiments. Indeed, ([Goldsmith and Heard 1961](#)) locate the top of the calcite-dolomite
613 solvus at a temperature of 1348 K and a composition of 43 mol% MgCO_3 . The variation of cell
614 parameters as a function of composition are in agreement with most previous studies
615 ([Bischoff et al. 1983](#); [Goldsmith et al. 1958](#); [Goldsmith et al. 1961](#)) but disagree with the results
616 of ([Zhang et al. 2010](#)) that strongly deviate from previous data, particularly above 30 mol%
617 MgCO_3 (*Fig. 1*).

618 The identification of two groups characterized either by narrow and symmetric peaks (low-Mg
619 synthetic calcites: MgCc2-MgCc26) or broadened and asymmetric peaks (high-Mg synthetic
620 calcites: MgCc28 to MgCc45) is of major importance and deserves further interpretation. First
621 of all, the features on which the separation into two groups are robust since (1) all MgCc above
622 26 mol% MgCO_3 display similar patterns, (2) higher temperatures (1373 K instead of 1273 K)
623 and pressure (1.5 GPa instead of 1 GPa) are not responsible for the peak widening because
624 two of the high-Mg calcites (MgCc28 and 30) synthesized at 1273 K, 1 GPa display similar broad
625 peaks. Actually, the broadening of the peaks corresponds to (1) a compositional variability in
626 the high-Mg calcites of the order of ± 1 mol% MgCO_3 , (2) a mean apparent strain $\langle \epsilon \rangle$ of about
627 4×10^{-3} against 2×10^{-4} in low Mg-calcites, (3) both effects of compositional heterogeneity. One
628 of them could be related to compositional variation between crystals as determined by EMP
629 of the order of ± 0.8 mol% MgCO_3 . But the second, finer level of compositional heterogeneity
630 could be due to the coexistence in a given crystal of coherent scattering domains, the
631 components of which have different cation ordering and slightly different compositions and
632 are producing microstructural strain. The actual distribution of Ca and Mg in each microcrystal

633 cannot be determined because the broadening of the diffraction peaks depends also on the
634 strain, size and distribution of the coherent scattering domains. Nanoscale heterogeneous
635 microstructures are very common in Ca rich dolomite natural samples. They were reported in
636 numerous HRTEM studies by interpreting HAADF image modulations and satellite reflections
637 in the diffraction patterns ([Fang and Xu 2019](#); [Larsson and Christy 2008](#); [Meike et al. 1988](#);
638 [Reksten 1990](#); [Shen et al. 2014](#); [Van Tendeloo et al. 1985](#); [Wenk et al. 1991](#)). But actually, if
639 many microstructures were proposed at the nanometric scale, no further structural details of
640 the domain model would be provided at the micrometric scale by single crystal diffraction
641 method ([Reeder 2000](#)) - *natural dolomites with 44 and 45.5 mol% MgCO₃ - S_{order} = 0.84 and*
642 *0.71*) and by comprehensive Rietveld techniques ([Drits et al. 2005](#)) *natural dolomites with*
643 *45.1, 47.8 and 48.4 mol% MgCO₃*). Considering all this, it is very likely that the constraints on
644 cation order in Ca rich dolomite similarly occur in the high-Mg synthetic calcite. Clearly, further
645 studies are required to validate the nanoscale compositional heterogeneity, but additional
646 valuable insights at the short-range-order scale could be given from our previous Raman data
647 ([Perrin et al. 2016](#)), as discussed below.
648

649 Length scales of the cationic disorder state

650 Unit-cell parameters and volume obtained for all the MgCc samples show small deviations
651 from the almost straight calcite-dolomite-magnesite line. Assuming that a total disordered
652 MgCc corresponds to an ideal solid solution and plots along the straight line, the strain
653 associated with the partial order (*p-ord*) - total disorder (*t-dis*) transformation is defined as ϵ_x
654 = $(X_{p-ord} - X_{t-dis}) / X_{t-dis} = \Delta X / X_{t-dis}$ where X_{p-ord} is the value of a , c or V obtained for a MgCc sample
655 and X_{t-dis} is the value of a , c or V calculated for the same composition from the straight line
656 through the end-members. The strains ϵ_a , ϵ_c , ϵ_v calculated for the a , c and V parameters, for
657 all the MgCc samples are plotted as a function of the Mg content in [Fig. 15](#).



658 **Fig. 15** Strain in magnesian calcites at RT as a function of Mg content a) ϵ_a ; b) ϵ_c ; c) ϵ_v ; (black: OCN
659 calcite and OCN dolomite; blue: low-Mg synthetic samples; red: high-Mg and MgCc50 synthetic
660 samples)

661 The strain values are negative for ε_a and ε_V and generally positive for ε_c ; they display different
662 behavior for low- and high-Mg synthetic calcites. In the range 0-22 mol% MgCO₃ (low-Mg:
663 MgCc2 to 26), all strain values increase as the Mg content increases, while in the high-Mg
664 synthetic calcites, ε_a and ε_V decrease, and ε_c increases. The transition between the two groups
665 is marked by a discontinuity (negative jumps for ε_a and ε_V , negative for ε_c). In the carbonate
666 structure, strongly bonded coplanar (CO₃)²⁻ groups are arranged parallel to the (0 0 1) plane
667 and connected through much weaker bonds to 6-coordinated divalent cations. Thus, the
668 negative strain along the *a* axis could be related to the distance O₁-O₂ of the MO₆ octahedra
669 (M=Ca or Mg), connecting two rigid (CO₃)²⁻ carbonate groups in the (0 0 1) plane. On the other
670 hand, the positive strain along the *c*-axis could be related to the variation of O₁-O₆ bond in
671 the MO₆ octahedra. Cation ordering affects the orientation of the (CO₃)²⁻ groups (1) by their
672 rotation (δ) around the *c* axis and (2) tilting out (γ) of the carbonate groups in the (0 0 1) plane.
673 The rotation generates a negative *a* strain, while tilting generates a positive *c* strain. On this
674 basis, both in-plane rotation (δ) and tilting out (γ) of the (CO₃)²⁻ groups increase as the Mg
675 content increases in the low-Mg calcites, whereas in-plane rotation (δ) decreases and tilting
676 out (γ) increases in the high-Mg calcites, as the Mg content increases. The basal rotation (δ)
677 and tilting out (γ) of the (CO₃)²⁻ groups are maximal at 25 and 50 Mg mol. %, respectively. The
678 above correlation indicates that the deviation with respect to an ideal solid solution in the
679 calcite-dolomite range is related to the local ordering or clustering of Ca and Mg in cation
680 layers involving reorientation of (CO₃)²⁻ groups, associated with an inverse strain of the unit
681 cell parameters, negative for *a* and positive for *c*.

682 Neither loss of rotational symmetry, nor long range cation ordering is observed by X-ray
683 diffraction in the synthetic magnesian calcites, only structural distortion. Thus partial ordering
684 can only be short-range. This conclusion is in agreement with the Raman study of the same
685 synthetic magnesian calcites reported in a previous study ([Perrin et al. 2016](#)). As shown in
686 [Supp. Mat. Fig. S6](#), the FWHMs of the Raman bands change as a function of Mg content and
687 type of vibrations within the (CO₃)²⁻ groups [bending deformation modes (doubly degenerate
688 Eg) that involve both carbon and oxygen motion, and stretching mode (A1g) which is like the
689 respiration mode of oxygen]. A comparison of [Figs. 15 and S6](#) shows that the unit cell strain
690 determined by XRD and the Raman band enlargement are correlated. The strain ε_a for the *a*
691 parameter ([Fig. 15a](#)) and the FWHM of the bending modes [particularly the internal
692 translation mode (T) ([Supp. Mat. Fig. S6a](#)) are similar]. On the other hand, the strain ε_c for the *c*
693 parameter ([Fig. 15b](#)) is more consistent with the enlargement observed for the single
694 stretching mode ν_1 ([Supp. Mat. Fig. S6e](#)). Below 25% Mg content, the heterogeneity between
695 local cationic configurations increases inside the crystals. Above 25% Mg content, the single
696 phase – multi-phase transition from homogeneous to heterogeneous crystals linked to the
697 strain relaxation is marked for both modes with a decrease of the local cationic configuration
698 heterogeneity towards dolomite like ordering. The heterogeneous MgCc crystals could be

699 made of different domains with different local ordering configurations having similar or
700 slightly different magnesium contents.

701 Thus, both the bending deformation and stretching modes observed by Raman spectroscopy
702 can be related to the two types of site-symmetry of the $(\text{CO}_3)^{2-}$ group: the off planar tilting (γ)
703 and the in plane rotation (δ), respectively. The genetic connection between the off plane tilting
704 (γ) specific to the dolomite structure and the stretching mode (ν_1 , A1g) is also supported by
705 the out of plane bending mode Raman peak (ν_2 , A2g). This peak, which is active in dolomite
706 structure, is weak in synthetic magnesian calcites but can be detected from about 10 mol. %
707 MgCO_3 and its intensity progressively increases thereafter until 50 mol% MgCO_3 ([Perrin et al.](#)
708 [2016](#)). As seen above, the synthetic MgCc50 dolomite is characterized by 36% cation
709 disordering in both types of cationic layers. No anomalous intensity (except for the *b*-type
710 reflection) nor FWHM broadening of the (*h k l*) peaks (potentially indicative of ordered
711 stacking sequence) were detected. The cation disordering corresponds to the maximal
712 positive strain of the *c* parameter. A medium negative strain of the *a* parameter is observed
713 ([Fig. 15](#)). Short-range disordering can be characterized from previous Raman data. As
714 observed in [Supp. Mat. Fig. S6](#), both enlargement of the stretching mode (ν_1 , A1g) and intensity
715 of the dolomite bending mode ($2\nu_2$, A2g) are maximal ([Fig. 7](#) in ([Perrin et al. 2016](#))), whereas
716 enlargements of the other bending modes start decreasing above 25 mol% MgCO_3 . Thus, the
717 short range Ca, Mg disorder set to 36% from $\sqrt{(I_{015}/I_{006})}$ order parameter, is characterized by
718 a decrease of the *a* parameter, an increase of the *c* parameter, and an increase of both in
719 plane rotation and off-plane tilting variability.

720

721 **Conclusion**

722 These data confirm the presence of an almost continuous solid-solution between calcite and
723 dolomite above 1273 K, and the presence of a second-order transition between long-range
724 disordered Mg calcite and dolomite in the interval 41-49 mol% MgCO_3 at 1373 K. In the Mg
725 calcites, the deviation from the Cc-Dol straight line in the *a*/Mg, *c*/Mg, or *V*/Mg diagrams is
726 interpreted in terms of cationic short-range ordering in the Mg calcites. This short-range order
727 is accompanied by in plane rotation and the off planar tilting of the $(\text{CO}_3)^{2-}$ groups in the anion
728 layer that are maximal at 25 and 50 Mg mol. %, respectively. As a result, the role of $(\text{CO}_3)^{2-}$
729 group ordering is an important factor in the crystal structure of Ca-Mg carbonate. The thermal
730 expansion of MgCc10, 24, 40 and 50 have been determined up to 650-750K. The thermal
731 expansivity deviates from the Cc-Dol straight line. Compared with calcite, dolomite and
732 magnesite previous results, this trend is interpreted in terms of interactive contributions of
733 CaO_6 and MgO_6 octahedra and CO_3 groups to the thermal expansion and thus explained by
734 the structural short-range ordering observed at RT. At higher temperatures complications
735 arise from cation reordering or partial decomposition of the samples. The excess of thermal
736 expansion coefficients from the Cc-Dol straight line are consistent with the thermal-structural
737 relationships proposed by ([Markgraf and Reeder 1985](#); [Reeder and Markgraf 1986](#)), and

738 supports the cationic short range ordering in the Mg calcites. The peak width of the
739 diffractograms allow separating the synthetic Mg calcites into two groups: low- and high-Mg
740 synthetic calcites. Low-Mg synthetic calcites are homogeneous in Mg content while high-Mg
741 synthetic calcites display domains with slight differences in Mg content and degree of short-
742 range order. The short-range Ca, Mg disorder could be at random or set into a mosaic of the
743 different planar ordering configurations reported in TEM studies for dolomite and Ca rich
744 dolomite ([Fang and Xu 2019](#); [Larsson and Christy 2008](#); [Meike et al. 1988](#); [Reksten 1990](#); [Shen
745 et al. 2014](#); [Van Tendeloo et al. 1985](#); [Wenk et al. 1983](#)) and by computer simulation approach
746 ([Burton and Van de Walle 2003](#); [Lacivita et al. 2017](#); [Reeder 2000](#); [Wang et al. 2011](#)). Further
747 studies are required to better characterize the size and spatial distribution of these domains.
748 One of the ways to quantify the local ordering state at the length scale of a few unit cells could
749 be to combine Z-contrast imaging from scanning transmission electron microscopy of
750 appropriate samples and image simulation, a novel approach developed by ([Fang and Xu
751 2019](#)). This new complete series of structural data on Mg calcite including thermal properties,
752 will serve as references in many fields of research involving synthetic crystals obtained in
753 solution-based crystallization processes (nanocrystals, mesocrystals, calcite/polymers
754 crystals), biogenic crystals and geological minerals. It will also provide a robust basis for studies
755 to come on the physical chemistry of precipitation, dissolution and ionic diffusion of Mg
756 carbonates, and for the thermodynamic modeling of solid solutions which is an important
757 research topic in many areas of materials science and geoscience.

758

759 **ACKNOWLEDGMENTS**

760 This work has been supported by the Centre National de la Recherche Scientifique (CNRS) –
761 Institut National des Sciences de l'Univers (INSU) through grant INTERRVIE 2017 to DV, by the
762 Agence Nationale pour la Recherche through ANR MOBi 2018, and by the Centre
763 Interdisciplinaire de Nanoscience de Marseille (CINaM) through internal grants. We would like
764 to thank A. Saül and A. Ricolleau for constructive discussions. This is contribution ANR MOBi
765 2. We are grateful to the European Synchrotron Radiation Facility for providing access to the
766 instruments and we would like to thank Andy Fitch for assistance in using beamline ID22.
767

768 **References**

- 769 Althoff PL (1977) Structural refinements of dolomite and a magnesian calcite and implications for
770 dolomite formation in marine environment *Am Mineral* 62 (7-8):772-783
771 Antao SM, Hassan I, Mulder WH, Lee PL, Toby BH (2009) In situ study of the R-3c to R-3m
772 orientational disorder in calcite. *Phys Chem Miner* 36 (3):159-169. doi:10.1007/s00269-008-
773 0266-y
774 Bischoff WD, Bishop FC, Mackenzie FT (1983) Biogenically produced magnesian calcite;
775 inhomogeneities in chemical and physical properties; comparison with synthetic phases. *Am
776 Mineral* 68 (11-12):1183-1188

777 Burton BP, Van de Walle A (2003) First-principles-based calculations of the CaCO₃–MgCO₃ and
778 CdCO₃–MgCO₃ subsolidus phase diagrams. *Phys Chem Miner* 30 (2):88-97.
779 doi:10.1007/s00269-002-0294-y

780 Byrnes AP, Wyllie PJ (1981) Subsolidus and melting relations for the join CaCO₃-MgCO₃ at 10 kbar.
781 *Geochim Cosmochim Acta* 45 (3):321-328. doi:[https://doi.org/10.1016/0016-7037\(81\)90242-](https://doi.org/10.1016/0016-7037(81)90242-8)
782 [8](https://doi.org/10.1016/0016-7037(81)90242-8)

783 Cowley JM (1950) An Approximate Theory of Order in Alloys. *Phys Rev* 77 (5):669-675.
784 doi:10.1103/PhysRev.77.669

785 Cowley JM (1960) Short- and Long-Range Order Parameters in Disordered Solid Solutions. *Phys Rev*
786 120 (5):1648-1657. doi:10.1103/PhysRev.120.1648

787 De Aza AH, Rodriguez MA, Rodriguez JL, De Aza S, Pena P, Convert P, Hansen T, Turrillas X (2002)
788 Decomposition of dolomite monitored by neutron thermodiffraction. *J Am Ceram Soc* 85
789 (4):881-888

790 Deelman JC (1999) Low-temperature nucleation of magnesite and dolomite. *Neues Jahrbuch Fur*
791 *Mineralogie-Monatshefte* (7):289-302

792 Deelman JC (2011) Low-temperature formation of Dolomite and Magnesite. Compact Disc
793 Publications Geology Series. Compact Disc Publications, Eindhoven, The Netherlands.
794 <http://www.jcdeelman.demon.nl/dolomite/bookprospectus.html>

795 Drits VA, McCarty DK, Sakharov B, Milliken KL (2005) New insight into structural and compositional
796 variability in some ancient excess-Ca dolomite. *Can Mineral* 43:1255-1290.
797 doi:10.2113/gscanmin.43.4.1255

798 Dubrovinsky L (2002) Thermal Expansion and Equation of State. In: Buschow KHJ, Cahn RW, Flemings
799 MC et al. (eds) *Encyclopedia of Materials: Science and Technology*. Elsevier, Oxford, pp 1-4.
800 doi:<https://doi.org/10.1016/B0-08-043152-6/01817-9>

801 Fang YH, Xu HF (2019) A new approach to quantify the ordering state of protodolomite using xrd,
802 tem, and z-contrast imaging. *Journal of Sedimentary Research* 89 (6):537-551.
803 doi:10.2110/jsr.2019.29

804 Fitch AN (2004) The high resolution powder diffraction beam line at ESRF. *Journal of Research of the*
805 *National Institute of Standards and Technology* 109 (1):133-142. doi:Doi
806 10.6028/Jres.109.010

807 Floquet N, Vielzeuf D, Ferry D, Ricolleau A, Heresanu V, Perrin J, Laporte D, Fitch AN (2015) Thermally
808 Induced Modifications and Phase Transformations of Red Coral Mg-Calcite Skeletons from
809 Infrared Spectroscopy and High Resolution Synchrotron Powder Diffraction Analyses. *Crystal*
810 *Growth & Design* 15 (8):3690-3706. doi:10.1021/acs.cgd.5b00291

811 Glover ED, Sippel RF (1967) Synthesis of magnesium calcites. *Geochim Cosmochim Acta* 31 (4):10.
812 doi:10.1016/0016-7037(67)90037-3

813 Goldsmith JR, Graf DL, Chodos AA, Joensuu OI, Mcvicker LD (1958) Relation between lattice constants
814 and composition of Ca-Mg carbonates. *Am Mineral* 43 (1-2):84-101

815 Goldsmith JR, Graf DL, Heard HC (1961) Lattice constants of the calcium magnesium carbonates. *Am*
816 *Mineral* 46 (3-4_Part_1):453-459

817 Goldsmith JR, Graf DL, Joensuu OI (1955) The occurrence of magnesian calcites in nature. *Geochim*
818 *Cosmochim Acta* 7 (5):212-230. doi:[https://doi.org/10.1016/0016-7037\(55\)90033-8](https://doi.org/10.1016/0016-7037(55)90033-8)

819 Goldsmith JR, Heard HC (1961) Subsolidus Phase Relations in the System CaCO₃-MgCO₃. *The Journal*
820 *of Geology* 69 (1):45-74. doi:10.1086/626715

821 Hammouda T, Andrault D, Koga K, T.Katsura, Martin A (2011) Ordering in double carbonates and
822 implications for processes at subduction zones. *Contrib Mineral Petrol* 161:439-450.
823 doi:10.1007/s00410-010-0541-z

824 Harker RI, Tuttle OF (1955) Studies in the system CaO-MgO-CO₂ ; Part 2, Limits of solid solution
825 along the binary join CaCO₃ -MgCO₃. *American Journal of Science* 253 (5):274-282.
826 doi:10.2475/ajs.253.5.274

827 Hashimoto H, Komaki E, Hayashi F, Uematsu T (1980) Partial decomposition of dolomite in CO₂. J
828 Solid State Chem 33 (2):181-188. doi:10.1016/0022-4596(80)90118-8

829 Irving AJ, Wyllie PJ (1975) Subsolidus and melting relationships for calcite, magnesite and the join
830 CaCO₃-MgCO₃ 36 kb. Geochim Cosmochim Acta 39 (1):35-53.
831 doi:[https://doi.org/10.1016/0016-7037\(75\)90183-0](https://doi.org/10.1016/0016-7037(75)90183-0)

832 Jenkins DM, Holmes ZF, Ishida K, Manuel PD (2018) Autocorrelation analysis of the infrared spectra
833 of synthetic and biogenic carbonates along the calcite–dolomite join. Phys Chem Miner 45
834 (6):563-574. doi:10.1007/s00269-018-0942-5

835 Lacivita V, D'Arco P, Mustapha S, Faria Bernardes D (2017) On the use of the symmetry-adapted
836 Monte Carlo for an effective sampling of large configuration spaces. The test cases of calcite
837 structured carbonates and melilites. Computational Materials Science 126:217-227.
838 doi:<https://doi.org/10.1016/j.commatsci.2016.09.037>

839 Larsson AK, Christy AG (2008) On twinning and microstructures in calcite and dolomite. Am Mineral
840 93 (1):103-113. doi:10.2138/am.2008.2520

841 Markgraf SA, Reeder RJ (1985) High temperature structure refinements of calcite and magnesite. Am
842 Mineral 70 (5-6):590-600

843 Maslen EN, Streltsov VA, Streltsova NR, Ishizawa N (1995) Electron density and optical anisotropy in
844 rhombohedral carbonates. III. Synchrotron X-ray studies of CaCO₃, MgCO₃ and MnCO₃. Acta
845 Crystallographica Section B 51 (6):929-939. doi:doi:10.1107/S0108768195006434

846 Meike A, Wenk HR, Okeefe MA, Gronsky R (1988) Atomic resolution microscopy of carbonates -
847 interpretation of contrast. Phys Chem Miner 15 (5):427-437. doi:10.1007/bf00311121

848 Merlini M, Sapelli F, Fumagalli P, Gatta GD, Lotti P, Tumiati S, Abdellatief M, Lausi A, Plaisier J,
849 Hanfland M, Crichton W, Chantel J, Guignard J, Meneghini C, Pavese A, Poli S (2016) High-
850 temperature and high-pressure behavior of carbonates in the ternary diagram CaCO₃-
851 MgCO₃-FeCO₃. Am Mineral 101 (6):1423-1430. doi:10.2138/am-2016-5458

852 Newton RC, Goldsmith JR, Smith JV (1969) Aragonite crystallization from strained calcite at reduced
853 pressures and its bearing on aragonite in low-grade metamorphism. Contrib Mineral Petrol
854 22 (4):335-348. doi:10.1007/BF00400128

855 Paquette J, Reeder RJ (1990) Single crystal X-ray structure refinements of 2 biogenic magnesian
856 calcite crystals Am Mineral 75 (9-10):1151-1158

857 Perrin J, Vielzeuf D, Laporte D, Ricolleau A, Rossman GR, Floquet N (2016) Raman characterization of
858 synthetic magnesian calcites. Am Mineral 101 (11):2525-2538. doi:10.2138/am-2016-5714

859 Putnis A (1992) An Introduction to Mineral Sciences. Cambridge University Press,

860 Radha AV, Kamath PV, Shivakumara C (2007) Order and disorder among the layered double
861 hydroxides: combined Rietveld and DIFFaX approach. Acta Crystallographica Section B 63
862 (2):243-250. doi:doi:10.1107/S010876810700122X

863 Reeder RJ (1983) Crystal chemistry of the rhombohedral carbonates. Reviews in Mineralogy and
864 Geochemistry 11 (1):1-47

865 Reeder RJ (1992) Carbonates; growth and alteration microstructures. Reviews in Mineralogy and
866 Geochemistry 27 (1):380-424

867 Reeder RJ (2000) Constraints on Cation Order in Calcium-rich Sedimentary Dolomite. Aquatic
868 Geochemistry 6 (2):213-226. doi:10.1023/a:1009659122772

869 Reeder RJ, Markgraf SA (1986) High-temperature crystal chemistry of dolomite. Am Mineral 71 (5-
870 6):795-804

871 Reeder RJ, Nakajima Y (1982) The nature of ordering and ordering defects in dolomite. Phys Chem
872 Miner 8 (1):29-35. doi:10.1007/BF00311160

873 Reeder RJ, Wenk H-R (1983) Structure refinements of some thermally disordered dolomites. Am
874 Mineral 68 (7-8):769-776

875 Reksten K (1990) Superstructures in calcite. Am Mineral 75 (7-8):807-812

876 Rietveld HM (1969) A Profile Refinement Method for Nuclear and Magnetic Structures. *J Appl*
877 *Crystallogr* 2:65

878 Rodriguez-Carvajal J (1993) FullProf: A Program for Rietveld Refinement and Profile Matching
879 Analysis of Complex Powder Diffraction Patterns (ILL). *Physica B* 192:55

880 Rodriguez-Navarro C, Kudlacz K, Ruiz-Agudo E (2012) The mechanism of thermal decomposition of
881 dolomite: New insights from 2D-XRD and TEM analyses. *Am Mineral* 97 (1):38-51.
882 doi:10.2138/am.2011.3813

883 Rodriguez-Navarro C, Ruiz-Agudo E, Nieto F, Livi KJT, Oberti R (2013) Carbonates: An overview of
884 recent TEM research. In: *Minerals at the Nanoscale*. Mineralogical Society of Great Britain
885 and Ireland, p 0. doi:10.1180/EMU-notes.14.10

886 Roisnel T, Rodriguez-Carvajal J (2001) WinPLOTR: A Windows tool for powder diffraction pattern
887 analysis. In: Delhez R, Mittemeijer EJ (eds) *Epdic 7: European Powder Diffraction, Pts 1 and 2,*
888 *vol 378-3*. Materials Science Forum. Trans Tech Publications Ltd, Zurich-Uetikon, pp 118-123.
889 doi:10.4028/www.scientific.net/MSF.378-381.118

890 Scherrer P (1918) Bestimmung der Grösse und der inneren Struktur von Kolloidteilchen mittels
891 Röntgenstrahlen. *Nachr Ges WissGöttingen* 26:98-100

892 Shen ZZ, Konishi H, Szlufarska I, Brown PE, Xu HF (2014) Z-contrast imaging and ab initio study on "d"
893 superstructure in sedimentary dolomite. *Am Mineral* 99 (7):1413-1419.
894 doi:10.2138/am.2014.4647

895 Stokes AR, Wilson AJC (1942) A method of calculating the integral breadths of Debye-Scherrer lines.
896 *Mathematical Proceedings of the Cambridge Philosophical Society* 38 (3):313-322.
897 doi:10.1017/S0305004100021988

898 Valverde JM, Perejon A, Medina S, Perez-Maqueda LA (2015) Thermal decomposition of dolomite
899 under CO₂: insights from TGA and in situ XRD analysis. *PCCP* 17 (44):30162-30176.
900 doi:10.1039/C5CP05596B

901 Van Tendeloo G, Wenk HR, Gronsky R (1985) Modulated structures in calcian dolomite - a study by
902 electron-microscopy. *Phys Chem Miner* 12 (6):333-341. doi:10.1007/bf00654343

903 Wang ML, Shi GH, Qin JQ, Bai Q (2018) Thermal behaviour of calcite-structure carbonates: a powder
904 X-ray diffraction study between 83 and 618K. *Eur J Mineral* 30 (5):939-949.
905 doi:10.1127/ejm/2018/0030-2768

906 Wang Q, Grau-Crespo R, de Leeuw NH (2011) Mixing Thermodynamics of the Calcite-Structured
907 (Mn,Ca)CO₃ Solid Solution: A Computer Simulation Study. *The Journal of Physical Chemistry*
908 *B* 115 (47):13854-13861. doi:10.1021/jp200378q

909 Warren BE, Averbach BL, Roberts BW (1951) Atomic Size Effect in the X-Ray Scattering by Alloys. *J*
910 *Appl Phys* 22 (12):1493-1496. doi:10.1063/1.1699898

911 Wenk H-R, Barber DJ, Reeder RJ (1983) Microstructures in carbonates. *Reviews in Mineralogy and*
912 *Geochemistry* 11 (1):301-367

913 Wenk HR, Hu MS, Lindsey T, Morris JW (1991) Superstructures in ankerite and calcite. *Phys Chem*
914 *Miner* 17 (6):527-539

915 Williamson GK, Hall WH (1953) X-ray line broadening from filed aluminium and wolfram. *Acta Metall*
916 *1* (1):22-31. doi:[https://doi.org/10.1016/0001-6160\(53\)90006-6](https://doi.org/10.1016/0001-6160(53)90006-6)

917 Zhang F, Xu H, Konishi H, Roden EE (2010) A relationship between d₁₀₄ value and composition in the
918 calcite-disordered dolomite solid-solution series. *Am Mineral* 95 (11-12):1650-1656.
919 doi:10.2138/am.2010.3414

920 Zucchini A, Comodi P, Katerinopoulou A, Balic-Zunic T, McCammon C, Frondini F (2012) Order–
921 disorder–reorder process in thermally treated dolomite samples: a combined powder and
922 single-crystal X-ray diffraction study. *Phys Chem Miner* 39 (4):319-328. doi:10.1007/s00269-
923 012-0489-9

924

